AFRL-RY-WP-TR-2016-0103

PIEZOELECTRIC NON LINEAR NANOMECHANICAL TEMPERATURE AND ACCELERATION INSENSITIVE CLOCKS (PENNTAC)

Gianluca Piazza
Carnegie Mellon University

Kimberly Turner
University of California Santa Barbara

Brian Otis
University of Washington

Todd Palmer
Vectron International

Valeriy Felmetsger
OEM Group

JULY 2016
Final Report

AIR FORCE RESEARCH LABORATORY
SENSORS DIRECTORATE
WRIGHT-PATTERSON AIR FORCE BASE, OH 45433-7320
AIR FORCE MATERIEL COMMAND
UNITED STATES AIR FORCE

NOTICE AND SIGNATURE PAGE

Using Government drawings, specifications, or other data included in this document for any purpose other than Government procurement does not in any way obligate the U.S. Government. The fact that the Government formulated or supplied the drawings, specifications, or other data does not license the holder or any other person or corporation; or convey any rights or permission to manufacture, use, or sell any patented invention that may relate to them.

This report is the result of contracted fundamental research deemed exempt from public affairs security and policy review in accordance with SAF/AQR memorandum dated 10 Dec 08 and AFRL/CA policy clarification memorandum dated 16 Jan 09. This report is available to the general public, including foreign nationals.

AFRL-RY-WP-TR-2016-0103 HAS BEEN REVIEWED AND IS APPROVED FOR PUBLICATION IN ACCORDANCE WITH ASSIGNED DISTRIBUTION STATEMENT.

// Signature//

DONALD L. AGRESTA
Program Manager
Electro-Optic Components Branch
Aerospace Components and Subsystems Division

// Signature//

MARK G. SCHMITT, Chief
Electro-Optic Components Branch
Aerospace Components and Subsystems Division

// Signature//

TODD W. BEARD
Deputy Chief
Aerospace Components and Subsystems Division
Sensors Directorate

This material is based on research sponsored by Air Force Research Laboratory (AFRL) and the Defense Advanced Research Agency (DARPA) under agreement number FA8650-12-1-7264. The U.S. Government is authorized to reproduce and distribute reprints for Governmental purposes notwithstanding any copyright notation thereon. The views and conclusions contained herein are those of the authors and should not be interpreted as necessarily representing the official policies or endorsements, either expressed or implied, of Air Force Research laboratory (AFRL) and the Defense Advanced Research Agency (DARPA) or the U.S. Government.

This report is published in the interest of scientific and technical information exchange, and its publication does not constitute the Government's approval or disapproval of its ideas or findings.

*Disseminated copies will show "//Signature//" stamped or typed above the signature blocks.

REPORT DOCUMENTATION PAGE

Form Approved
OMB No. 0704-0188

1. REPORT DATE *(DD-MM-YY)*	2. REPORT TYPE	3. DATES COVERED *(From - To)*
July 2016	Final	20 August 2012 – 20 March 2016

4. TITLE AND SUBTITLE
PIEZOELECTRIC NON LINEAR NANOMECHANICAL TEMPERATURE AND ACCELERATION INSENSITIVE CLOCKS (PENNTAC)

5a. CONTRACT NUMBER
FA8650-12-1-7264

5b. GRANT NUMBER

5c. PROGRAM ELEMENT NUMBER
61101E

6. AUTHOR(S)
Gianluca Piazza (Carnegie Mellon University)
Kimberly Turner (University of California Santa Barbara)
Brian Otis (University of Washington)
Todd Palmer (Vectron International)
Valeriy Felmetsger (OEM Group)

5d. PROJECT NUMBER
1000

5e. TASK NUMBER
N/A

5f. WORK UNIT NUMBER
Y0U2

7. PERFORMING ORGANIZATION NAME(S) AND ADDRESS(ES)

Carnegie Mellon University
5000 Forbes Ave.
Pittsburg, PA 15213-3815

University of California Santa Barbara
University of Washington
Vectron International
OEM Group

8. PERFORMING ORGANIZATION REPORT NUMBER

9. SPONSORING/MONITORING AGENCY NAME(S) AND ADDRESS(ES)

Air Force Research Laboratory
Sensors Directorate
Wright-Patterson Air Force Base, OH 45433-7320
Air Force Materiel Command
United States Air Force

Defense Advanced Research Projects Agency/DARPA/MTO
675 N Randolph Street
Arlington, VA 22203

10. SPONSORING/MONITORING AGENCY ACRONYM(S)
AFRL/RYDP

11. SPONSORING/MONITORING AGENCY REPORT NUMBER(S)
AFRL-RY-WP-TR-2016-0103

12. DISTRIBUTION/AVAILABILITY STATEMENT
Approved for public release; distribution is unlimited.

13. SUPPLEMENTARY NOTES
The U.S. Government is joint author of the work and has the right to use, modify, reproduce, release, perform, display or disclose the work. This report is the result of contracted fundamental research deemed exempt from public affairs security and policy review in accordance with SAF/AQR memorandum dated 10 Dec 08 and AFRL/CA policy clarification memorandum dated 16 Jan 09. Report contains color.

14. ABSTRACT
Besides the phase noise (PN) requirement in wireless applications such as Wi-Fi, Bluetooth, and GPS, frequency stability under temperature change is also a very important specification that needs to be satisfied. Although the introduced oscillator using microelectromechanical systems (MEMS) based resonator helps to lower PN and achieve high figure of merit compared to other state-of-the art oscillators, the resonator is the main contributor for frequency variation according to the temperature change. The work accomplished during this effort demonstrated the first fully integrated oven control system to mitigate the temperature effect on the reference clock. It showed low frequency drift (1.5ppm) with the highest resolution sensor (150uK), which meets the most stringent requirement for GPS application. As this system does not require any calibration on the MEMS resonator because of its feedback structure, there is benefit from its characteristics of short test time and time-to-market. It can also lead to lower cost from the product perspective.

15. SUBJECT TERMS
phase noise, microelectromechanical systems, contour mode resonator

16. SECURITY CLASSIFICATION OF:			17. LIMITATION OF ABSTRACT:	18. NUMBER OF PAGES	19a. NAME OF RESPONSIBLE PERSON (Monitor)
a. REPORT	b. ABSTRACT	c. THIS PAGE			Don Agresta
Unclassified	Unclassified	Unclassified	SAR	72	19b. TELEPHONE NUMBER *(Include Area Code)* N/A

Table of Contents

Section **Page**

List of Figures

Figure **Page**

Figure **Page**

Figure **Page**

List of Tables

Table **Page**

1.0 SUMMARY

During the project period, our team has tackled the main challenges related to the demonstration of low noise and high frequency miniaturized aluminum nitride (AlN)-based frequency sources. In earlier phases, we have understood non-linearity in AlN contour-mode resonators operating at frequencies ranging from 100 MHz to few GHz and demonstrated oscillators with outstanding temperature stability and acceleration sensitivity. In later phases, we have especially focused on understanding the damping and noise sources in our oscillators and identifying new methods to evade phase noise. Briefly, we summarize in bullet form the main accomplishments and contributions made in understanding and engineering miniaturized frequency sources.

1) Demonstrated the ability to use parametric bifurcation to filter and shape the noise of a 227 MHz AlN oscillator. ***The resulting phase noise (PN) at 1 kHz offset scaled to a 1 GHz carrier is - 111 dBc/Hz***.

2) Identified the origin of elastic nonlinearities in AlN contour mode resonators (CMRs). The nonlinear behavior is due to thermal effects when the resonators are electrically excited and the input is slowly (slow with respect to the device thermal time constant) swept through the excitation frequencies close to the main resonance.

3) Demonstrated the ability to use duffing non-linearities in AlN resonators to cancel amplifier phase noise below the thermal time constant of the resonator. Practical demonstration is described by theoretical model. This demonstration can be broadly applied to other non-linear resonators.

4) Built a low PN autonomous parametric oscillator based on a 226.7 MHz AlN CMR. ***This topology enables an improvement in the phase noise of 16 dB at 1 kHz offset with respect to a conventional feedback-loop oscillator based on the same device. The method is broadly applicable to any frequency source.***

5) Identified frequency flicker noise in the AlN resonator as the main PN limiting mechanism when a low noise amplifier is used. A non-linear model describing the resonator noise was generated and imported into a standard circuit simulator.

6) Developed a frequency fluctuation measurement technique using a vector network analyzer. We also demonstrated a residual noise reduction in AlN CMRs by prolonged radio frequency (RF) excitation ("burn-in" effect)

7) Developed a homodyne noise detection setup to measure flicker noise of individual resonators, which is later formulated into the equivalent closed loop phase noise that an oscillator would exhibit if it were to be built with such a resonator. ***The resonator PN directly depends on damping in resonators.***

8) Identified major source of damping in high frequency AlN contour-mode resonators. Anchor losses are dominant for frequencies in the range of 200-300 MHz, whereas thermoelastic damping (TED) dominates above 750 MHz. Segmented electrodes were introduced to reduce damping without affecting the resonator transduction efficiency.

9) Identified that the use of an optimized size of the inactive region permits to minimize the acoustic energy lost through the anchors. In combination with electrode shaping, we demonstrated Qs approaching 4,000 at 1 GHz in air.

10) Temperature compensation via resonator ovenization was experimentally demonstrated. Two methods of using ovenization were implemented and demonstrated. ***A final temperature stability of < 2 ppm from – 40 to + 85 °C was demonstrated for a microcontroller based ovenized oscillator***.

11) Integrated AlN CMRs to a colpitts oscillator with on-chip temperature compensation method. ***A PN as low as -121.6 dBc/Hz was measured for a Colpitts oscillator with AlN CMR. The overall circuit fits in an area of 1.5x 2 mm^2.***

12) ***An acceleration sensitivity < 40 ppb/G was recorded for vibration frequencies between 100 Hz and 2 kHz***. Acceleration sensitivity < 1 ppb/G was recorded for the higher vibration frequencies. We have identified the major sources of acceleration sensitivity to be in the component mounting and wirebonds.

Overall, the project has enabled significant advancements in the field of micro/nanomechanical oscillators. In depth understanding of non-linearity, damping and noise will have a long-lasting impact that goes beyond the specifics of this program as it broadly applies to resonant devices used for inertial, physical and gravimetric sensing. A high degree of miniaturization and low power consumption has been demonstrated. Thanks to this program it is possible to envision the deployment of frequency sources that have performance comparable to the one of quartz crystals, but occupying a fraction of the volume (100x of the smallest quartz crystal oscillators) and consuming about 3 order of magnitude lower power. Furthermore, operation in high-G environments (about 1 to 2 orders of magnitude higher than what quartz crystals can do) will be made possible if electronics and mechanical resonators are tightly integrated, something that is not at all possible with quartz crystals. Future efforts should focus on the direct or 3D integration of the AlN contour-mode resonators with electronics and the development of methods for enabling large tuning and frequency programmability.

In the following sections, the various accomplishments of the program are reported in more detail.

2.0 METHODS, ASSUMPTIONS, AND PROCEDURES

2.1 Parametric Bifurcation Enables Phase Noise Filtering

We excite parametric bifurcation in a parametric divider formed by a non-linear varactor and two parallel tanks set a ω_0 and $2\omega_0$, ω_0 being the oscillator carrier frequency (Figure 1). The parametric divider is placed at the output of the AlN resonator based oscillator. The oscillator output frequency is first doubled and its magnitude amplified prior to feeding the parametric divider. A second loop taking the output of the parametric divider and feeding the signal back to the amplifier is also introduced to reduce the amplifier dc-power needed to activate the division. A parametric divider is a 2-port network that transfers energy from an input signal at ω to an output signal at $\omega/2$. Above a certain input power a system pole becomes unstable and a flip-type bifurcation occurs. The unstable pole causes the rising of a sub-harmonic oscillation. This activation power is mostly set by the varactor dc-bias, V_{dc}, and by the input power, $P_{in}(2\omega_0)$. Considering the parametric circuit (Figure 1), and using the voltage across the varactor, $v(t)$, as the only state variable, it is possible to define a complex admittance, $Y_T(\omega_0)$, as functions of $P_{in}(2\omega_0)$ and V_{dc}:

$$Y_T(\omega_0) = Y_T(P_{in}(2\omega_0), 2\omega_0, V_{dc}) \quad (1)$$

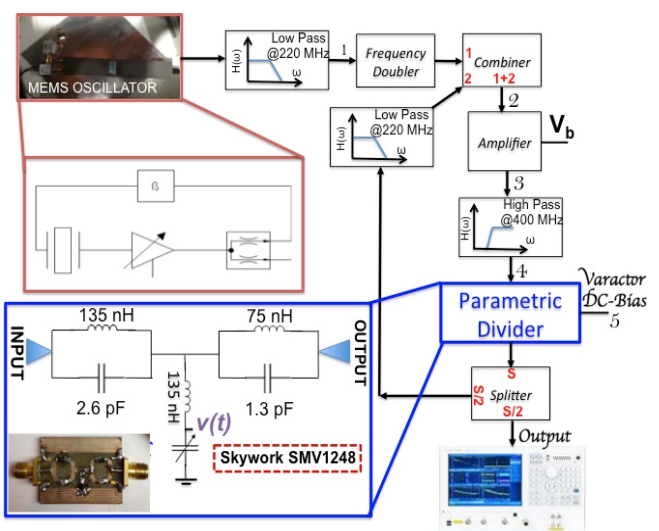

Figure 1: Parametric Filtering Topology used to Reduce Oscillator PN

The output at ω_0 of the feedback-loop oscillator, based on a 227 MHz AlN resonator, is filtered around the oscillation frequency and sent to a frequency doubler (1). The output of the frequency doubler is amplified (2), filtered (3), and sent to the parametric divider input (4). The varactor direct current (DC)-bias, V_{dc}, and the divider input power, P_{in}, regulated by the amplifier bias voltage, V_b, sets the divider working point. Half of the divider output is sent to the output load. The other half is sent back to the input of the amplifier (2) to reduce the amplifier DC-power consumption.

Under the assumption that $Y_T(\omega_0)$ is real close to the division threshold, and no white noise is added by the divider circuit, the spectrum of the PN of the sub-harmonic oscillation, $\Delta\varphi_T(\Omega)$, where Ω is the frequency offset is given by:

$$|\Delta\varphi_T(\Omega)|^2 = \frac{[\frac{dY_T}{d\varphi}]^2 \cdot [\varphi_s(\Omega)/2]^2}{[\frac{dY_T}{d\varphi}]^2 + [\frac{dY_T}{d\omega}]^2 \cdot \Omega^2} \quad (2)$$

Eq. (2) shows that for small Ω the PN of the divider tends to the linear prediction (φs(Ω)/2). For larger Ω (> 10-100 Hz) and especially for a large derivative of the admittance with respect to frequency, the second term at the denominator plays a key role. By regulating the varactor DC-bias it is possible to modify the divider working point and make it operate close to the bifurcation region, where $dY_T/d\omega$ is maximized. Effectively, this phenomenon enables reduction of the oscillator PN because the divider is not able to track the fast noise perturbations of the microelectromechanical systems (MEMS) oscillator. In the case of a 227 MHz AlN oscillator, this technique brought > 26 dB improvement in the PN at Ω =10 kHz offset and > 20 dB improvement at Ω =1 kHz offset (Figures 2-3). This technique yields a PN of –124 dBc/Hz at 1 kHz offset for a 227 MHz carrier. Referenced to a 1 GHz carrier, this PN corresponds to -111 dBc/Hz. To our knowledge this is the lowest PN ever reported for any MEMS based oscillator. The demonstrated technique is of general value and could be applied to any MEMS oscillator.

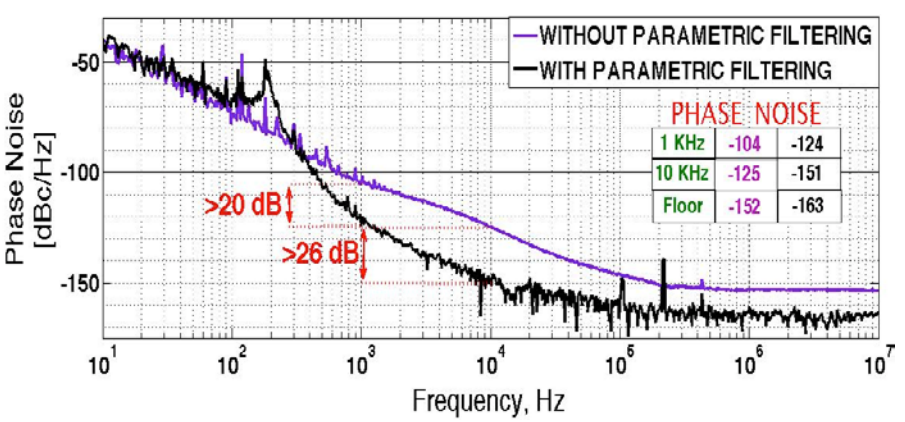

Figure 2: Purple: PN for the Feedback Loop 227 MHz Oscillator without Parametric Filtering and Black: PN at the Output of the Parametric Filter when V_{dc} is 2.07 V and V_b=16V
In this case the system is working close to the division bifurcation.

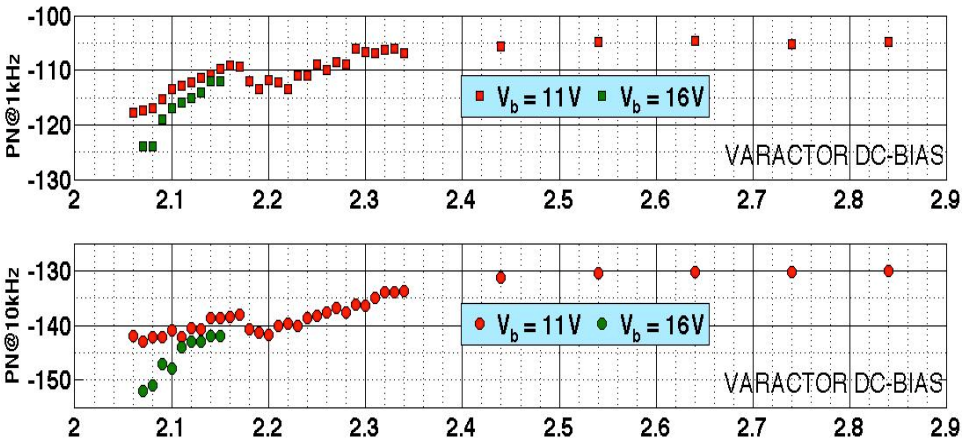

Figure 3: Squares: PN at 1 kHz Offset for Different Varactor DC-biases and for Two Distinct Amplifier Bias Voltages, V_b (Figure 1) and Circles: PN at 10 kHz Offset for Different Reverse Varactor DC-biases and for Two Distinct Amplifier Bias Voltages, V_b (Figure 1)

In the case in which V_b=16V, the sub-harmonic oscillation occurs for a much narrower range of varactor DC-biases (2.07 - 2.15 V). When no parametric filtering is used the phase noise is - 104 dBc/Hz at 1 kHz offset and -125 dBc/Hz at 10 kHz offset. Instead, the use of parametric filtering enables 20 dB improvement in the phase noise at Ω=1 kHz and 26 dB at Ω=10 kHz.

2.2 Duffing Resonator Cancels Amplifier Noise

Here, we consider the complete dynamic model of a self-heating AlN resonator and analyzed the response of the resonator to a frequency sweep through resonance and its relationship to the sweep rate. In addition, we illustrate that while the self-heating nonlinearity appears similar to the Duffing nonlinearity in the quasi-static case, its dynamics are different. This has important implications, especially related to the ability of these resonators to evade amplifier noise in oscillators.

We introduced a non-liner resonator model (Figure 4), which describes the first order dependence of the mechanical (motional) components (R_m, L_m, C_m) on temperature. The resonator is described by the following set of differential equations:

$$\begin{aligned} L_m\ddot{q}_m + (R_m + R_s)\,\dot{q}_m + \frac{1}{C_m}q_m &= V - R_s\dot{q}_0, \\ (R_0 + R_s)\dot{q}_0 + \frac{1}{C_0}q_0 &= V - R_s\dot{q}_m, \\ C_{\text{th}}\dot{T} + \frac{T}{R_{\text{th}}} &\approx (R_m^{(0)} + R_s)\dot{q}_m^2. \end{aligned} \tag{3}$$

where

$$L_m \approx L_m^{(0)} + L_m^{(1)} T,$$
$$R_m \approx R_m^{(0)} + R_m^{(1)} T,$$
$$C_m \approx C_m^{(0)} + C_m^{(1)} T.$$

By solving this set of equations, we were able to accurately predict the resonator response when excited by an external network analyzer for different signal sweep rates (Figure 5). These results imply that we can correctly picture the resonator dynamics and use the aforementioned model in a closed-loop oscillator to predict phase noise shaping in the presence of strong non-linearities.

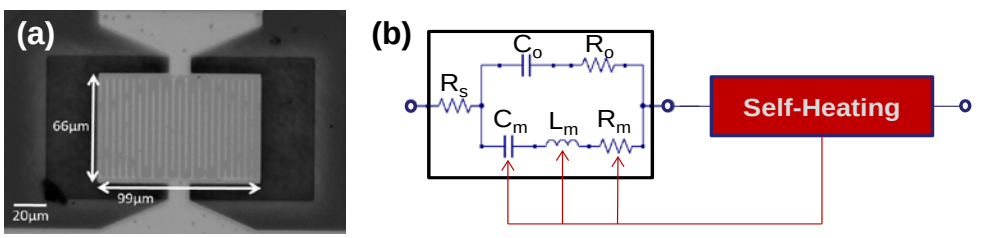

Figure 4: (a) Microscope Image of a 1 GHz AlN Contour-Mode Resonator and (b) Modified Butterworth Van Dyke (MBVD) Circuit Model with Nonlinear Motional Elements

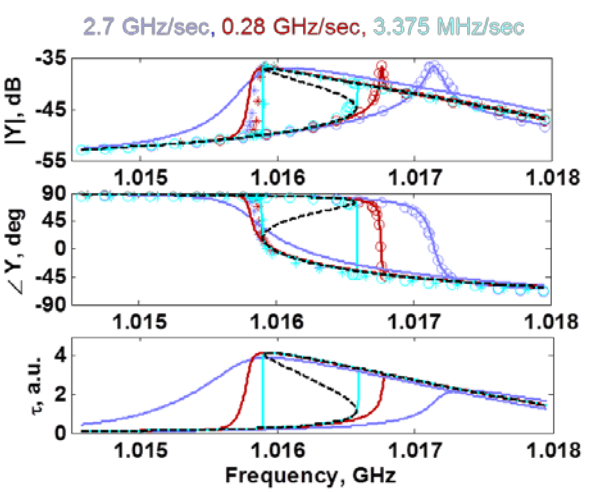

Figure 5: Experimental (discrete points) and Fitted (continuous line) Response (respectively from top to bottom: admittance magnitude, admittance phase, and resonator temperature) of a 1 GHz AlN CMRs for Different Input Signal Sweep Rates

The input power was kept constant at 11 dBm. It is evident that the resonator behavior depends on the sweep rate, a clear sign that its dynamics are regulated by the device thermal time constant. The overlaid dashed black line represents the fixed point solution of the Duffing resonator.

Resonator non-linearities tend to worsen the oscillator PN by converting amplitude noise to frequency noise. Nonetheless, this non-linear phenomenon can also be exploited for evading amplifier phase fluctuations. In fact, a non-linear resonator exhibits specific phase/frequency relationship for which the oscillator dynamics can be substantially modified. Intuitively, the resonator time constant can be made infinite at special operating points generated by the resonator non-linearity. When the resonator is locked in that particular state in a closed-loop oscillator, then the amplifier phase fluctuations can be eliminated. To prove this theory we have built a 222 MHz oscillator using coaxial electronic components (Figure 6 (top)). In this case, the AlN CMR is mounted on a 2-port printed circuit board (PCB) (Figure 6 (bottom)) that is connected in series with the rest of the components in the circuit. All the discrete elements, SMA connectors, and cables are chosen to have the characteristic impedance equal to 50 Ω for matching purposes. An external DC power supply is used to bias the RF amplifier (Mini-circuits ZKL-1R5+) and the output is taken from one of the power divider (M/A-COM T-1000) terminals. To close the loop, one terminal is connected to the phase shifter (ATM P1213). In this particular implementation, the selected amplifier was characterized by a large intrinsic $1/f^2$ noise.

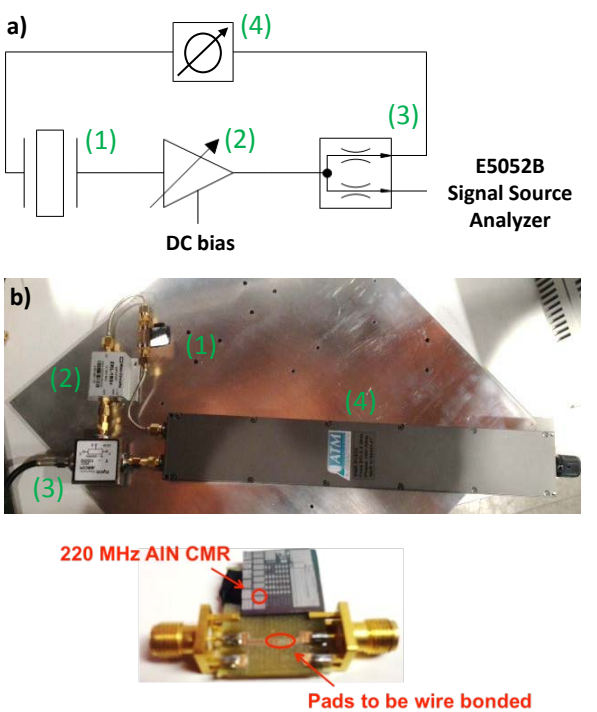

Figure 6: Schematic and Actual Implementation of the Oscillator Setup used to Demonstrate PN Shaping via a Duffing Resonator (top) and Photograph of 222MHz AlN CMR Wire Bonded on a 2-Port FR4 Circuit Board (bottom)

(1) AlN CMR mounted on a PCB, (2) RF amplifier, (3) power divider, and (4) phase shifter.

When driving the resonator non-linearly (by means of sufficient gain) and tuning the loop phase, it was possible to identify specific working points that yielded a significant phase noise reduction (Figure 7). The PN reduction was limited to frequency offsets below the resonator thermal time constant. The obtained results can be fit by theoretical predictions. It is important to note that PN cancellation occurs only for noise sources external to the resonator. When the noise source is intrinsic to the resonator (see next section) this technique is not applicable. Nonetheless, the practical demonstration is of general interest in proving the use of non-linearity for shaping phase noise. Our team has ultimately used a different approach based on parametric filtering to meet the stringent phase noise requirements dictated by the Defense Advanced Research Agency (DARPA) program.

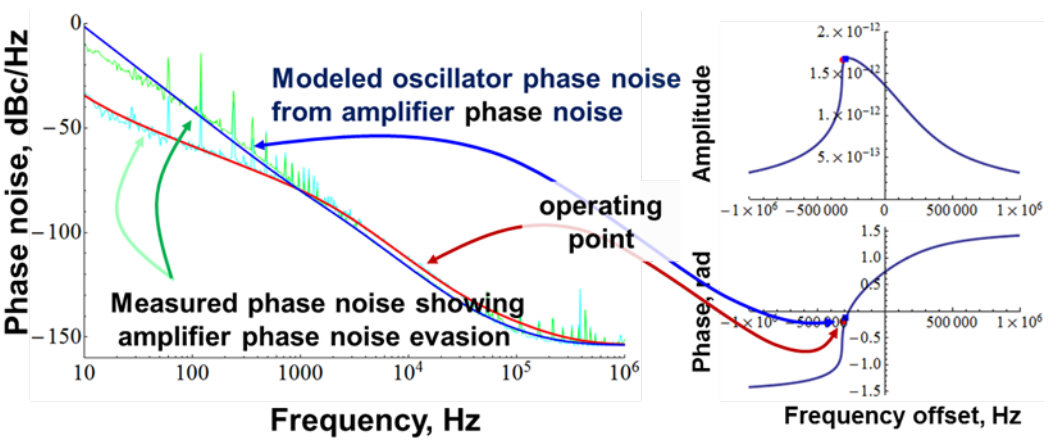

Figure 7: Measured PN Response of the Non-linear 222 MHz AlN Oscillator for Different Phase Conditions (green and light blue curves) and Predicted PN Response is Overlapped (blue and red curves)

It is clear that the oscillator PN is reduced for particular amplitude and phase conditions exhibited by the Duffing resonator.

2.3 Low Phase Noise Autonomous Parametric Oscillator

The non-linear dynamics of a non-autonomous parametric oscillator were exploited as a powerful tool to enable phase noise reduction in a MEMS-based oscillator. When the resonator employed in an oscillator circuit is parametrically driven (i.e., its stiffness is modulated at twice the oscillation frequency), the oscillator steady state solution is less sensitive to phase fluctuations affecting the circuit components. Parametric modulation has been used in this work to enable phase noise reduction in a MEMS piezoelectric-based oscillator operating in the microwave frequency range.

The oscillator presented in this work (Figure 8) is based on the use of a capacitive degenerate parametric amplifier working in its division range. A 226.7 MHz aluminum nitride contour-mode resonator is connected at the so-called signal terminal of the parametric amplifier (Figure 9). A low pass filter and an external amplifier follow the resonator. The output of amplifier 1 is plugged into the input port of a resistive 3 dB power splitter. One of the two output ports of the power splitter is sent to a signal source analyzer for measurement. The other port of the power splitter is sent to a frequency doubler, which has a minimum

conversion loss of 13 dB at the frequency of interest. The output of the frequency doubler is sent to a second external amplifier. The dc bias of amplifier 2 is labeled as *V*a and will be varied to study its impact on the parametric oscillator response. The signal from amplifier 2 is connected to a phase shifter and a low-pass filter. The output of the filter feeds the input of the parametric amplifier through the RF-port of a bias-T that is also used to reverse bias the variable capacitor, in the parametric amplifier, with voltage, *V*bias.

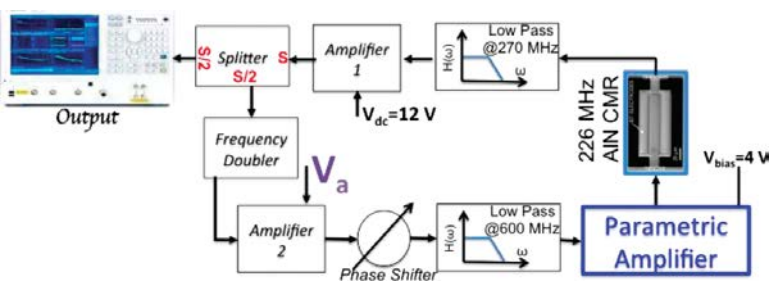

Figure 8: Schematic Representation of the Oscillator Topology
A parametric amplifier and a frequency doubler are inserted in a conventional feedback loop oscillator based on a 226.7 MHz AlN contour-mode resonator.

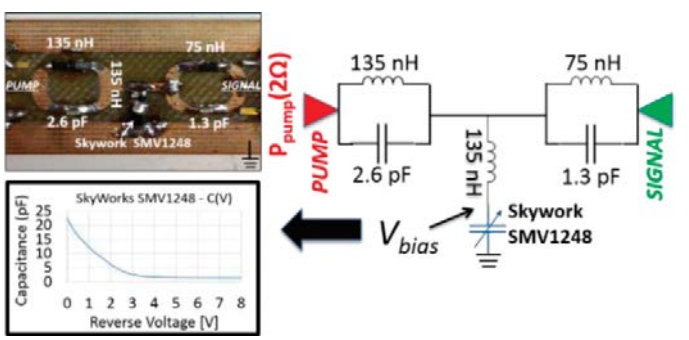

Figure 9: Parametric Amplifier Designed and Built for this Work
The varactor's C(V) characteristic is also reported.

The parametric amplifier circuit (Figure 9) includes two notch filters, placed at the pump and signal ports, a variable capacitor and a stabilization inductor placed in series to the variable capacitor. The notch filters permit reduction of the portion of pump and output energy, respectively, leaking through signal and output ports. The notch filter placed at the pump port was conveniently designed to resonate at a slightly larger frequency than the resonance frequency of the CMR that is employed in the oscillator circuit. This choice permits reduction of the sensitivity of P_{th} to un-modeled parasitics. Similarly, a second notch filter was placed at the signal port. The resonance frequency of this filter was set to be approximately two times the resonance frequency of the notch filter connected at the pump port. The variable capacitor was selected to achieve a high parametric gain at the frequency of interest. A hyper abrupt varactor was used because of its wide tuning range and moderate capacitance value (~ 5 pF) with respect to other available varactor technologies. The proper selection of the stabilization inductor is crucial to achieve low P_{th}. To find its optimum value we recurred to frequency-domain simulations run in a commercial circuit simulator (Agilent ADS).

The complete circuit schematic we adopted in the simulation is shown in Figure 10. It is well known [8] that the performance of parametric circuits depends largely on the output load connected at the signal port. Because our ultimate goal was to optimize the performance of the parametric amplifier when used in the oscillator circuit (Figure 8), we connected the signal port of the amplifier to an impedance equivalent to the one seen in the oscillator circuit. This was done by including the CMR and the lowpass filter electrical models in series to the 50 Ω matched input impedance of amplifier 1 in the circuit model. The simulation permitted finding the stabilization inductance value (~135 nH) that minimizes P_{th}. The same analysis was used to predict the parametric amplifier response for different P_{pump} values (Figure 11).

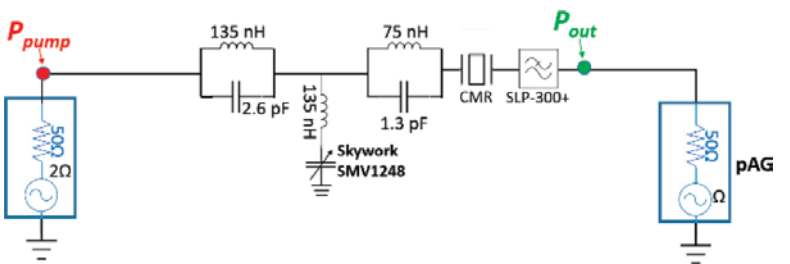

Figure 10: Circuit Schematic used to simulate the Parametrically Generated Sub-Harmonic Frequency through a Commercial HB Simulator

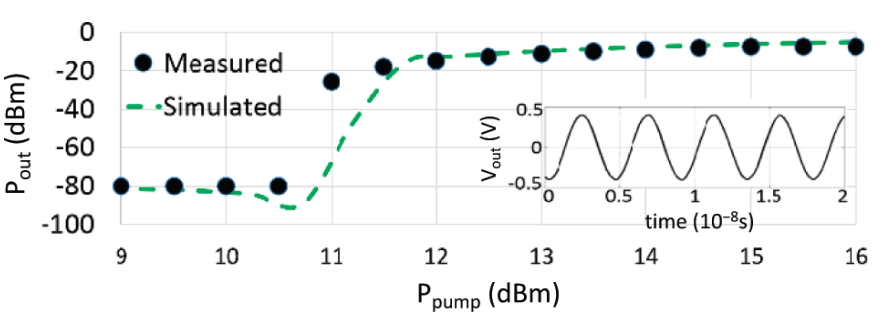

Figure 11: Parametric Amplifier Response for different P_{pump} Values

Black dots: measured Pout at 226.7 MHz for different pump power levels and Vbias equal to 4 V. This dc value was chosen to ensure that the varactor operates far enough from its forward conduction, but still exhibits low P_{th}. In green (dashed line): simulated Pout at 226.7 MHz through HB simulation run in Agilent ADS. Inset: output voltage waveform measured across the 50 Ω output load when P_{pump} was set to be 16 dBm. It is evident that the output voltage shows an almost pure sinusoidal signal with a frequency equal to 226.7 MHz.

We measured the spectrum of these fluctuations in the resonator we used for the parametric oscillator. This was done via an open-loop noise measurement (Figure 12). The measurement revealed that the resonator frequency fluctuations have a 1/f spectrum, indicative of flicker frequency noise. The measured frequency noise was used to analytically predict the phase noise we would measure in a closed-loop oscillator, if the phase fluctuations coming from the circuit were to be evaded. This noise was compared with the best measured phase noise of the feedback-loop oscillator obtained by removing the frequency doubler and parametric amplifier from the oscillator circuit. The measured phase noise is larger than the analytical prediction which considers noise coming only from the resonator. This experiment proves that circuit noise

dominates over the frequency noise of the resonator and justifies using parametric amplification to reduce the oscillator noise.

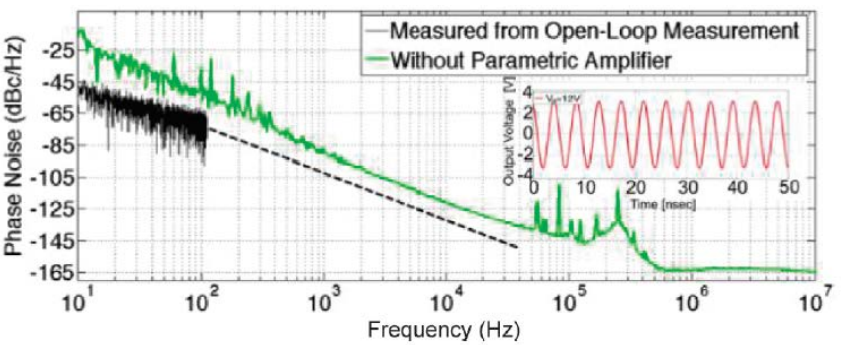

Figure 12: Black: Closed-loop PN Predicted by Open-loop Measurement of the Resonator Frequency Fluctuations and Green: Best PN Measured without a Parametric Amplifier

Part of the black curve was measured (continuous line) and the remainder (>100 Hz) is extrapolated (dashed line).

The best PN we measured at the output of the parametric oscillator is compared, in Figure 13 (blue curve), to the best PN of the conventional feedback loop oscillator. As evident, this curve matches the PN analytically predicted (Figure 13, black curve) by considering the measured frequency noise of the CMR as the main noise source in the loop. This fact proves that the oscillator PN is now limited by the resonator noise and that cancellation of the circuit noise was achieved. An improvement of more than 16 dB at 1 kHz offset was obtained by using the new oscillator topology rather than the conventional configuration.

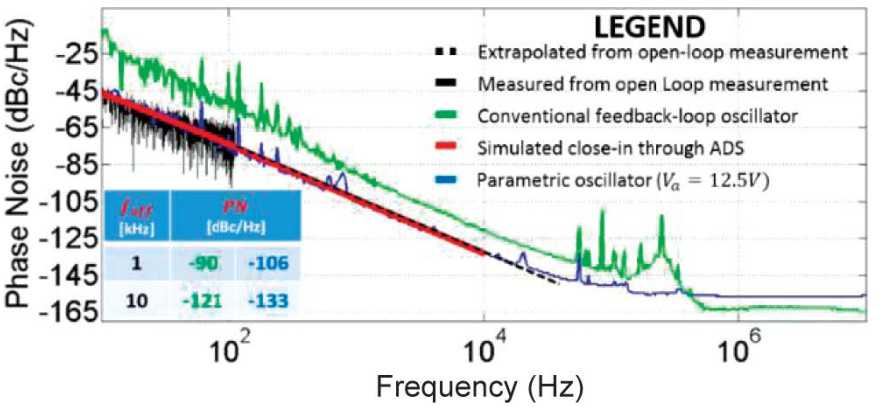

Figure 13: Best PN Measured at the Output of the Parametric Oscillator Compared to the Best PN of the Conventional Feedback Loop Oscillator

In black: predicted closed-loop phase noise by open-loop measurement of the resonator frequency fluctuations. Part of this curve was measured (continuous line) and the remainder (>100 Hz) is extrapolated (dashed line). In green: best phase noise measured using the conventional feedback-loop oscillator, Va was set to 12 V and the output power was 14 dBm. In red: simulated phase noise, in the close-in region, through Agilent ADS. In blue: best phase noise we measured in the parametric oscillator. Va is set to 12 V and the output power is 12.5 dBm. Both the measured curves were evaluated at one output port of the power splitter following amplifier 1.

2.4 Vector Network Analyzer Measurement of Frequency Fluctuations in AlN CMRs

In order to engineer high performance and low PN oscillators it is essential to understand the frequency fluctuations present in the resonator. These fluctuations contribute directly to the phase noise of the closed-loop oscillator and set the lower bound of achievable PN levels in any oscillator where the resonator serves as the frequency reference. Unlike PN arising in the amplifier, resonator frequency fluctuations cannot be evaded by employing bending in the frequency response found in Duffing and similar nonlinear resonators.

Here, we introduce a frequency fluctuation measurement technique using a vector network analyzer (VNA), an interferometric measurement tool that is commonly already a part of any RF laboratory's toolset. This technique allows a rather rapid and precise measurement of frequency fluctuation of individual AlN CMRs. In more detail, we examine a generalized quasi-static model as well as a more detailed dynamic model and compare on- and two-port measurement setups. More information on theoretical models can be found in: N. Miller and G. Piazza, *2013 Joint UFFC, EFTF and PFM Symposium.*

For the measurement, we consider a 473 MHz one-port AlN CMR measured by an Agilent N5230A vector network analyzer. In order to measure the intrinsic frequency fluctuations of the resonator, the resonator was driven in continuous wave (CW) mode at resonance, 473 MHz. In order to characterize the VNA the VNA source phase noise was measured using the Agilent E5052B signal source analyzer. The PN spectrum is shown in Figure 14 in green. In addition a passive attenuator was measured using the VNA. The attenuation was similar to the loss in the resonator reflection coefficient and so the phase fluctuations of the attenuator measurement should provide a valid measure of the VNA measurement noise floor. Moreover, if we compare

the VNA measurement noise to the PN of the VNA source we find the VNA PN is much lower and thus negligible.

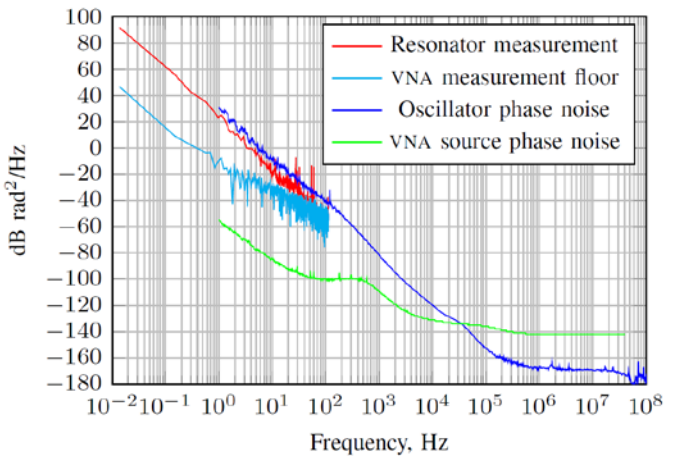

Figure 14: Spectrum of PN for the Oscillator, the Resonator Measured in Open-loop, the VNA Source, and a Passive Attenuator used to determine the Measurement Noise Floor

Next we measured the resonator, performing 9 CW sweeps of 16001 points with a sampling frequency and IF band width of 200 Hz. The power spectral density of the frequency fluctuations was then calculated using the follow equation:

$$S_{\angle\Gamma}(\omega) = \left(\frac{\partial\angle\Gamma}{\partial\Omega}\bigg|_{\omega_0}\right)^2 \left(S_\Omega(\omega) + S_{\omega_0}(\omega)\right) + S_m(\omega) \tag{4}$$

which ignores the source frequency fluctuations and the measurement noise, and averages over the multiple CW sweeps. S_Ω is the power spectral density of the drive frequency fluctuations, $S_{\omega o}$ is the power spectral density of the resonator frequency, and, S_m is the measurement noise spectrum. As a point of comparison, the same oscillator was placed into an oscillator and the phase noise of that oscillator was measured using the E5052B. Figure 14 shows both the oscillator PN and the resonator frequency fluctuations, referred to phase by division by ω^2. It is clear that the measurement noise floor (cyan) is well below the measured resonator noise (red). The resonator noise (red) is matched in slope and only 5-10 dB below the closed-loop oscillator PN (blue). This comparison supports the validity of the proposed measurement technique.

2.5 Noise Reduction in AlN CMRs by Prolonged RF Excitation

Very low PN oscillators are highly desirable for military radar applications. In order to improve phase noise performance of MEMS oscillators, it is essential to reduce the residual noise of the resonator, which serves as the frequency selective element. The oscillator closed loop PN is typically limited by the 1/f flicker noise intrinsic to the MEMS resonator acting as the frequency selective element. In this work, the ability to reduce the 1/f flicker noise and consequently the residual PN of 1GHz MEMS AlN CMR by prolonged exposure to RF power at resonant frequency is explored.

For experiment, we measure residual noise of one-port AlN CMRs using the above VNA-based measurement technique. After measuring the resonator's initial residual noise, a CW signal close to resonant frequency is chosen with the desired RF power level to drive the device and produce the "burn-in" effect. An amplifier was used for RF power levels above +10 dBm. The resonator's S11 response and residual noise is then measured again post burn-in.

The power spectral density (PSD) of the closed loop phase noise for "pre" (before burn-in) and "post" (after burn-in) of a sample AlN CMR device is shown in Figure 15. The device was exposed to an incident RF power of +10 dBm close to resonant frequency for a period of 2 hours and the closed loop noise was then measured after performing the burn-in procedure. An improvement of about 20 dBc/Hz was observed at an offset frequency of 1 Hz. The improvement in phase noise is noted by performing a linear fit to the closed loop noise before and after burn-in. As seen from Figure 15, the closed loop noise has $1/f^3$ slope, which translates to a 1/f slope in the open loop case (indicative of flicker noise). The slope of closed loop PN remains unchanged after burn-in as seen in Figure 15.

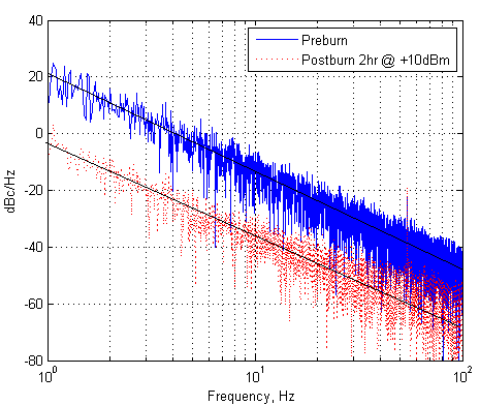

Figure 15: Closed Loop PN, S_φ, for an AlN CMR before (blue trace) and after (red trace) Exposure to +10dBm RF Power at Resonant Frequency for 2 hours

It was found by experiment that a RF power of either +10 dBm for a period of 2 hours or a +16 dBm for 1 hour had a similar effect for devices at 1 GHz. Power levels higher than +16 dBm caused irreversible damage in the device and severely degraded the Q. In general, the burn-in produced a slight increase in Q and showed a permanent reduction in the PN of the resonator. There were, however, some instances in which the burn-in resulted in either no improvement in phase noise or an increase in PN in some cases. Figure 16 is a plot of the measured Q versus predicted closed loop PN of several one-port AlN CMRs before and after burn-in. The diamonds are pre-burn-in values and the squares represent the post-burn-in value. Each pre/post burn-in device pair is labeled with an alphabet ranging from A to Q and the plot shows that after the burn-in procedure most devices show an improvement in Q and a decrease in the closed loop PN.

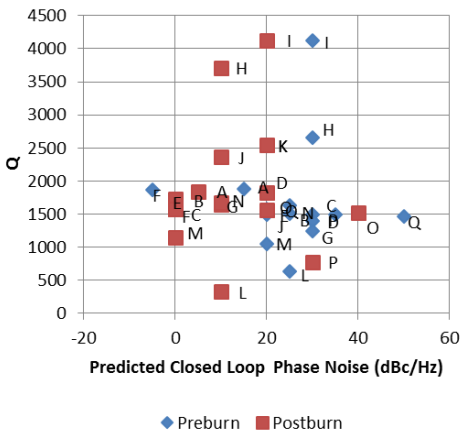

Figure 16: Plot of the Measured Q versus Predicted Closed Loop PN of Several One-port AlN CMRs before and after Burn-in

The diamonds are pre-burn-in values and the squares represent the post-burn-in values.

Figure 17 is a plot of the change in resonator Q versus change in closed loop PN of the devices "post" burn-in. In Figure 17, most resonators show an increase in *Q* after the burn-in procedure. The change in *Q* corresponded to a decrease in the motional resistance of the resonator extracted from fitting the resonator admittance to the MBVD model.

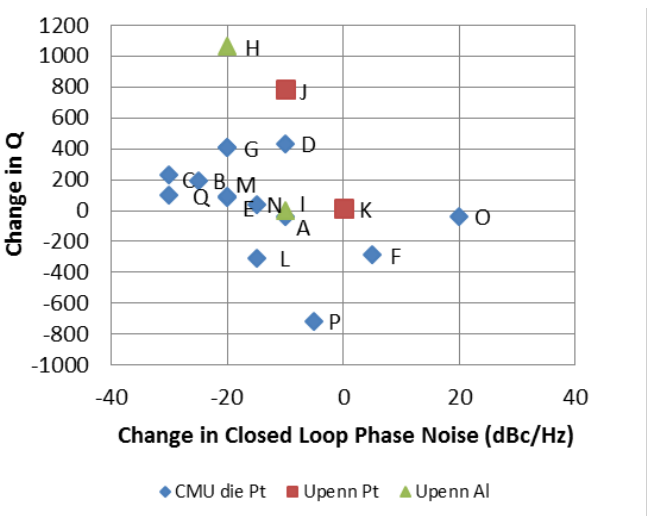

Figure 17: Change in Resonator Q versus Change in Closed Loop PN of the Devices "Post" Burn-in

The trend for most devices is that an increase in Q was observed as well as a decrease in the closed loop phase noise.

2.6 Impact of Damping on Flicker Frequency Noise of AlN CMRs

Here, we study the effect of damping on flicker frequency (1/f) noise of 1.1 GHz AlN CMRs. A total of 52 different AlN-CMRs are systemically designed and fabricated to give quality factors (Q_U) ranging from 300 to 3500, allowing the study of how two major damping mechanisms in AlN-CMRs, 1) anchor losses and 2) TED, affect the resonator 1/f noise. In total, we have measured 104 CMRs and the results confirm that 1/f noise shows a clear power law dependence that is close to $1/Q^3$, independently of the main nature of the damping mechanism.

Extensive studies on improving the resonator Q have revealed that the two main damping mechanisms for AlN-CMRs are 1) anchor losses, which is the mechanical energy loss through the anchor that connects the resonator to the substrate, and 2) TED inside the top and bottom electrodes. Since each damping mechanism can be modeled and accounted for at the resonator design level, AlN-CMRs allow a systemic study on how different damping mechanisms impact the resonator 1/f noise.

To analyze the effect of two major damping mechanisms of anchors losses and TED on the resonator 1/f noise, 52 different AlN-CMRs were fabricated with varying device parameters, as shown in Table 1. Device parameters were systemically designed by means of finite element analysis and analytical methods to attain a broad range of Qs. To vary anchor losses, we controlled the length of the electrodes (E_L) and fabricated devices with different anchor types, labelled as full anchor and narrow anchor devices. For TED control, we varied the width of the top electrodes (E_W) to change the electrode coverage area of CMRs.

Figure 18(a) shows that Q_U increases with E_L, indicating that the effect of anchor losses decreases as E_L increases. It also shows that Q_U is higher for the narrow anchor devices than the full anchor devices E_L is less than 52 μm. However, the change in Q_U becomes small for longer devices because the acoustic wavelength (λ = 8 μm) becomes small compared to E_L and TED dominates the resonator damping. Figure 18(b) shows that Q_U decreases when E_W increases. This is because TED increases with the amount of metal. By systemically designing AlN-CMRs with different parameters, we have successfully fabricated a set of devices with Q_U ranging from 300 to 3500, where a broad range of Q_U is clearly affected by anchor losses for shorter devices ($E_L < 52$ μm) and by both anchor losses and TED for longer devices ($E_L \geq 52$ μm).

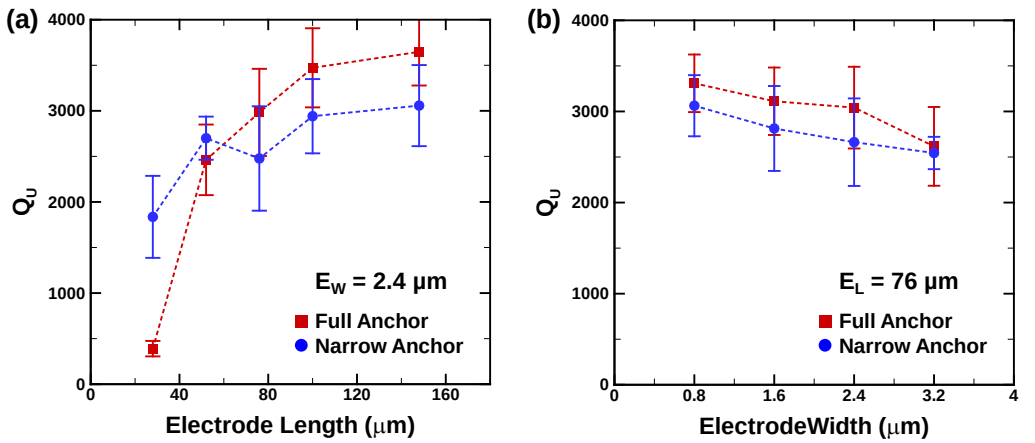

Figure 18: Unloaded Q_U as Functions of (a) E_L and (b) E_W
A wide range of Q_U, from 300 to 3500, is achieved.

Figure 19(a) illustrates the homodyne test setup that is used to directly measure the 1/f noise of AlN-CMRs. This setup can make additive noise measurements on active and passive microwave devices. Frist, a signal from the source is split into a phase shifter and a CMR. To operate the CMRs in the linear regime, an attenuator is used to keep the input power lower than -5 dBm. The output signal from a CMR is then amplified and input into the RF port of the mixer. Another split signal passes through the phase shifter and the delay is adjusted so that the two mixer inputs are in quadrature, giving the output to be proportional to the phase difference between the two signals. The output from the mixer is then filtered through a low pass filter and the resulting baseband noise is measured using a signal source analyzer (Aglilent E5052B). This approach cancels the close-in flicker frequency noise from the voltage source and therefore allows a precise and rapid measurement of the resonator 1/f noise. The noise floor of the setup is excellent, as shown in Figure 19(b).

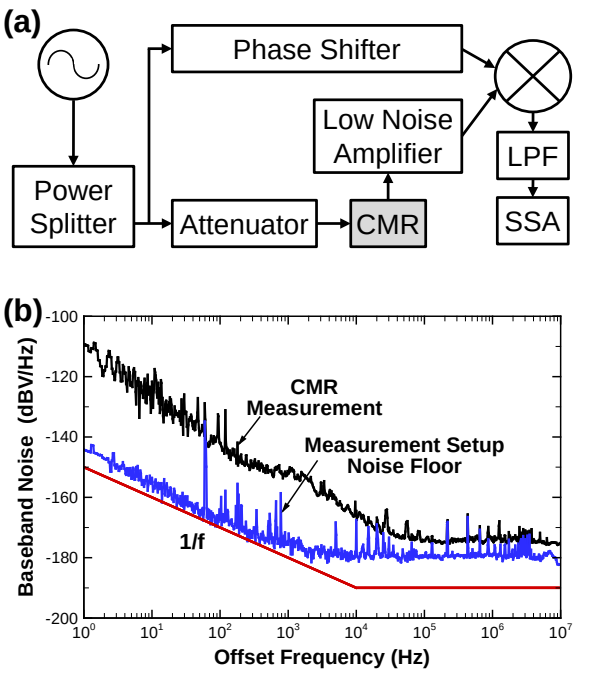

Figure 19: (a) Schematic of the Homodyne Setup that is used to Measure the Baseband Noise of AlN-CMRs and (b) Measured Baseband Noise of the Test Setup and a CMR, which clearly Follow the 1/f Trend

In order to compare the obtained noise values to meaningful data reported in the literature for oscillators, we converted 1/f noise into the equivalent closed loop phase noise, $L(f)$, that an oscillator would exhibit if it were to be built with such a resonator. The measured baseband noise, $S_V(f)$, is the voltage PSD due to phase fluctuation introduced by the resonator frequency fluctuations. The PSD of resonator frequency fluctuations, $S_{\varphi(f)}(f)$ can be then calculated as:

$$S_{\varphi(f)}(f) = \frac{S_V(f)}{2K^2G^2}\left[\frac{f_0}{2Q}\right]^2 \tag{5}$$

where K is the mixer gain constant, G is the gain applied to the baseband signal prior to measurement by the signal source analyzer, and f_0 is the resonant frequency of the device. The PSD of the resonator frequency fluctuation can then be converted to the PSD of a closed loop PN, $L(f)$, as below:

$$L(f) = S_{\varphi(f)}(f)\left[\frac{1}{f}\right]^2 \tag{6}$$

where f is the offset frequency from the main carrier. The predicted $L(f)$ of a resonator using the homodyne method matches well with the PN measurement of an oscillator containing the same resonator (difference is less than 5 dB). Furthermore, the $L(f)$ of the setup noise floor is predicted to be -120 dBc/Hz at 1 kHz offset, which is significantly lower than the measured $L(f)$ of 1 GHz AlN-CMRs, which is in the range of

-60 dBc/Hz to -90 dBc/Hz. In this work, we report L(f) values at 1 kHz offset from the carrier frequency because it is an important metric in many wireless systems.

Using the homodyne noise detection setup, we have measured the 1/f noise of a total of 104 AlN-CMRs (52 CMRs each from two different chips). Figure 20 shows the predicted L(f) at 1 kHz carrier frequency offset as a function of Q_U. It is clear that L(f) decreases as Q_U increases. Overall, the resonator 1/f noise follows the power law dependence of $1/Q_U^{2.74}$ with a relatively strong correlation (R^2 = 0.67). CMRs exhibit similar L(f) for a given Q_U regardless of the anchor types, indicating that the resonator 1/f noise depends on the intrinsic Q_U of the device. For this study, the lowest L(f) is measured to be -91 dBc/Hz at 1 kHz carrier frequency offset for a resonator with Q_U of about 3300.

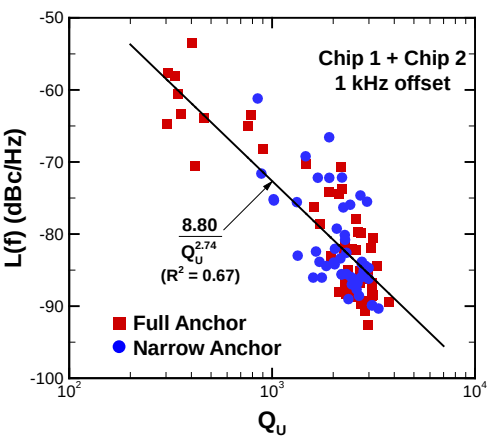

Figure 20: L(f) of all Measured CMRs from Two Different Chips
L(f) shows a clear power law dependence that is close to $1/Q_U^3$.

Our results confirm that damping directly impacts the 1/f noise of AlN-CMRs. However, the exhibited power law dependency of L(f) to Q for AlN-CMRs, which is $1/Q^3$, differs from the previously reported values for quartz crystal resonators of about $1/Q^4$, where it is assumed that the fluctuation in relaxation time associated with the phonon scattering inside the quartz crystal dominates the 1/f noise [2]. This discrepancy might be due to the fundamental difference in quartz crystal resonators and AlN-CMRs, such as the type of piezoelectric or electrode materials, the range of operating frequencies, and the active volume of devices. Thus, perhaps a different model or analysis should be applied to understand the 1/f noise mechanism for AlN-CMRs or other types of MEMS resonators.

For 1.1 GHz AlN-CMRs, TED in the top and bottom electrodes ultimately limits the resonator Q. In contrast, anchor losses can be largely mitigated by fabricating longer CMRs (where $E_L >> \lambda$). Thus, improving the electrode designs to alleviate TED should further enhance the noise performance of AlN CMRs. It has been demonstrated that a stress induced annealing of AlN-CMRs by driving them with high RF power improved Q and decreased the residual noise of the device. This is believed due to the change in grain size of metal electrodes and dislocations of the AlN film. Similarly, an annealing also improved the noise performance of quartz surface acoustic wave (SAW) resonators. Thermal annealing of metals at high temperatures (i.e.

400 °C for Al) induces a grain growth, and thus could be a good way to study the effect of grain size of the metal electrodes on the resonator *Q* and 1/f noise. This will be the subject of future work.

2.7 Impact of Thermoelastic Damping on Resonator Noise

A recent study has experimentally verified that the main intrinsic material damping in AlN CMRs is of thermodynamic nature and concludes that it comes primarily from TED in the top and bottom metal electrodes, especially for high-frequency CMRs. At low temperatures, TED is mitigated due to the decreased fluctuation in the temperature field inside the electrodes, and thus improving the device *Q*. To investigate the relationship between the resonator *Q* and flicker noise when TED is largely mitigated, we measured a total of 25 resonators (11 full-anchor and 14 narrow-anchor devices) at 10 K using Lakeshore cryogenic probe station. For the measurement, we only considered the resonator designs where the device *Q* is mostly affected by TED and not anchor losses.

Figure 21 shows the noise floor of our homodyne measurement setup at different environmental conditions of in ambient air, under vacuum at room temperature and at 10 K. We converted the measured baseband noise into the single sideband (SSB) PN by assuming a resonator *Q* of 2000. The noise floor of the measurement setup in Lakeshore probe station is excellent and can measure the phase noise of as low as -110 dBc/Hz at 1 kHz offset from the carrier frequency. There are some unidentified fluctuations in the noise floor from 100 Hz to 10 kHz offset frequencies, which might be originated from the cryogenic compressor or the large temperature gradient across the probe and the resonator pads at such low temperatures.

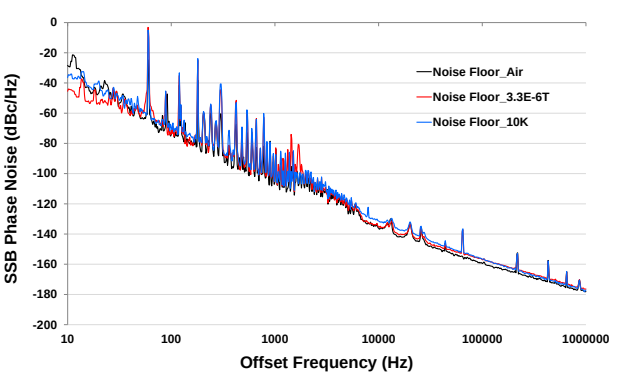

Figure 21: Noise Floor of the Homodyne Test Setup Integrated into Lakeshore Cryogenic Probe Station

The noise floor is consistent for different environmental conditions of in air, under vacuum at room temperature, and under vacuum at 10 K.

Figure 22 shows the resonator Q_U and $L(f)$ of a resonator in ambient air and under vacuum at 10 K. As expected, the resonator Q_U dramatically increased from 2486 to 6286 as the temperature decreased from room temperature to 10 K, this is because TED becomes negligible in cryogenic temperatures [5]. In addition, $L(f)$ decreased from -79.8 dBc/Hz to -99.1 dBc/Hz along with the temperature, further verifying that the resonator *Q* indeed impacts flicker noise of the device.

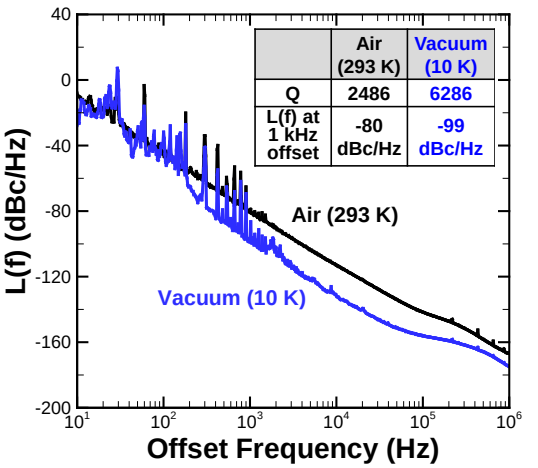

Figure 22: L(f) as a Function of an Offset Frequency for a Full-Anchor AlN CMR
Q_U increases and L(f) decreases when the temperature decreases from 293 K to 10 K.

After validating the noise measurement setup with Lakeshore probe station, we measured a total of 25 AlN CMRs (11 full-anchor devices and 14 narrow-anchor devices) from chip 1under vacuum at 10 K. For selecting the device for measurements, we excluded the ones where the anchor loss is the dominant damping mechanism. Figure 23(a) shows the L(f) of AlN CMRs at the temperature of 10K, where the lowest L(f) is measured to be -102 dBc/Hz at 1 kHz offset from the carrier frequency for the device with Q_U of about 5100. This is more than 10 dBc/Hz improvement compared to the L(f) measured in ambient air for the same device. Overall, the resonator flicker noise follows the power law dependence of $1/Q_U^{3.27}$. For comparison, we combined the noise data collected at 10 K with the previously measured data at 293 K for the resonators from the same chip, as shown in Figure 23(b). Clearly, the measurements at 10 K follow the trend that is observed in ambient environment; exhibiting the power law dependency where L(f) scales with $1/Q_U^3$. This result indicates that the intrinsic Q_U of the resonator sets the noise level of the device, regardless to the main nature of the damping mechanism. Hence, enhancing the resonator Q is critical to improve the noise performance of AlN CMRs.

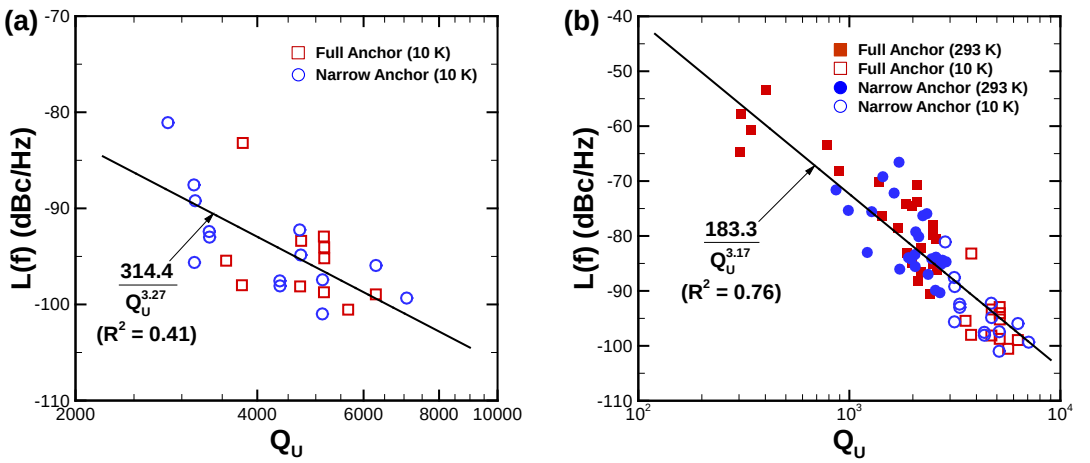

Figure 23: L(f) as a Function of Q_U of AlN CMRs (a) Under Vacuum at 10 K and (b) in Air at 293 K and in Vacuum at 10 K

L(f) decreases significantly at a lower temperature.

One other way to achieve different *Q*s for a resonator with the same device parameter is changing the electrode material. TED mostly depends on the thermal properties of the metal, and thus using different metal electrodes would exert different amount of TED on the resonator and ultimately determining the device *Q*. For this study, we fabricated a set of AlN CMRs having three different top electrode metals of Pt, Au, and Al (all 100-nm-thick), with a 100-nm-thick Pt bottom electrode and a 1-µm-thick AlN layer.

Figure 24 shows the Q_U obtained over the resonators (all full-anchor devices) with different top electrode materials. Figure 24(a) shows that Q_U decreases when E_W increases. This is because TED increases with the amount of metal [5]. Figure 8(b) shows that Q_U increases with E_L, indicating that the effect of anchor losses decreases as E_L increases. The change in Q_U becomes small for longer devices because the acoustic wavelength ($\lambda = 8$ µm) becomes small compared to E_L and TED dominates the resonator damping. All of our measurement shows that Al top electrode exhibits the larges Q_U while Pt top electrode induces the smallest Q_U, indicating that the type of metal indeed affects the damping in the resonator. For devices with EL = 24 µm, Q_U is consistent at about 500 regardless to the type of top electrode material, and this is because the resonator *Q* is mostly limited by anchor losses for shorter devices.

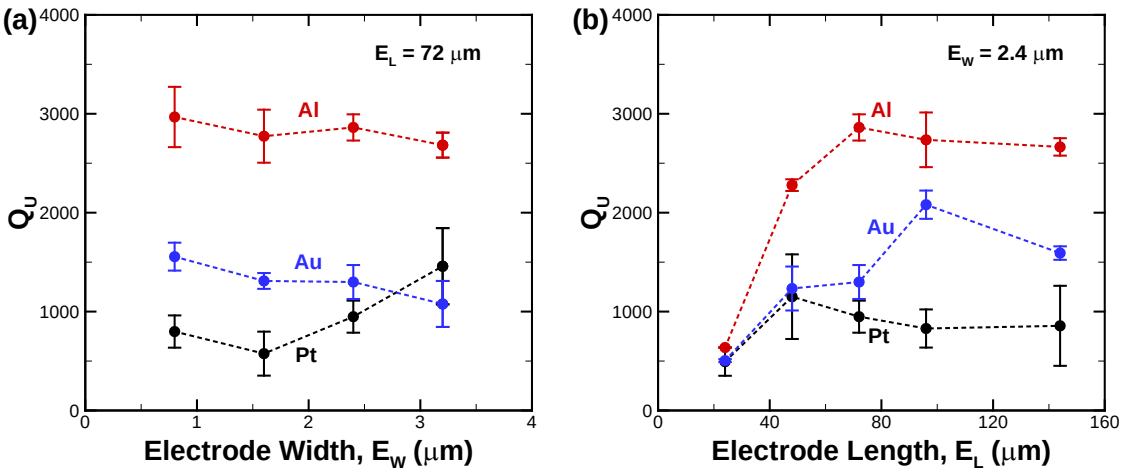

Figure 24: Q_U of Full-anchor AlN CMRs as Functions of (a) E_W and (b) E_L
Resonators with Al top electrode exhibit the highest Q_U while Pt stop electrode gives the lowest Q_U value.

To understand the effect of metal electrodes on the resonator noise, we measured the noise of 22 additional resonators, 12 for Pt and 10 for Au top electrodes, and compared the result with the previous measurements on the resonators with Al top electrodes (35 devices, Figure 25). All devices are fully anchored. For the measurement, we only considered the devices those are clearly affected by TED (i.e. $E_L \geq 52$ μm). Figure 25 shows the measurement data and it shows that $L(f)$ decreases as Q_U increases for all three different top electrode metals. The trend follows what we have observed from previous studies. $L(f)$ follows a power law dependence that ranges from $1/Q_U^{3.2}$ to $1/Q_U^{3.8}$.

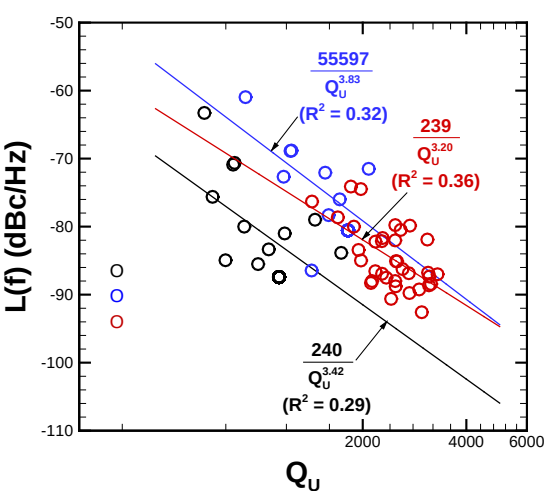

Figure 25: Noise Measurement of CMRs with Different Top Metal Electrodes of Pt, Au, and Al

2.8 Mitigation of Anchor Losses in AlN Contour-Mode Resonators

Here, we analyze possible sources of dissipation in AlN CMRs for three different resonance frequency devices (*fr*) (220 MHz, 370 MHz, and 1.05 GHz). For this purpose, anchors of different widths (*Wa*) and lengths (*La*) proportional to the acoustic wavelength (λ) are designed as supports for resonators in which the dimensions of the vibrating body are kept fixed. The *Q* extracted experimentally confirms that anchor losses are the dominant source of damping for most anchor designs when *fr* is equal to 220 and 370 MHz. For specific anchor dimensions (Wa/λ is in the range of 1/4–1/2) that mitigate energy leakage through the supports, a temperature-dependent dissipation mechanism dominates as seen in higher *fr* resonators operating close to 1.05 GHz. To describe the *Q* due to anchor losses, we use a finite-element method with absorbing boundary conditions. In this way, we are able to quantitatively predict *Q* due to anchor losses and qualitatively describe the trends observed experimentally.

We have systematically studied the behavior of 324 devices having a fixed AlN plate size (60x144 μm), operating at 3 different frequencies (220, 370 and 1050 MHz), and having variable anchor size (function of the acoustic wavelength, λ). Each particular condition was tested in 9 separate devices so that meaningful statistics could be collected. The experimental results are shown in Figure 26. It is evident that anchor losses (energy escaping through the resonator supports) play a dominant role at frequencies in the range of 200-300 MHz. At higher frequencies, the resonator damping is instead dominated by interfacial dissipation (due to a stress jump occurring at the interface between the AlN film and the electrodes).

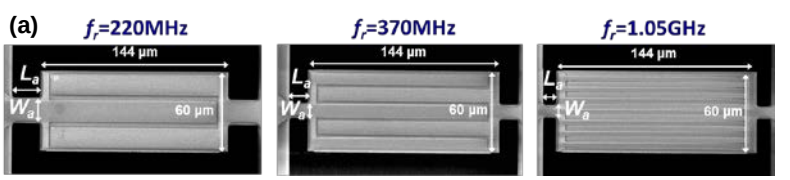

(b)

		Quality factor					
		fs=220MHz		fs=370MHz		fs=1.05GHz	
Wa/λ	La/λ	Avg	Stand Dev	Avg	Stand Dev	Avg	Stand Dev
1/4	1/4	1532	448	1424	500		
1/2	1/4	2343	1014	1468	694	1331	510
1	1/4	520	150	667	267	1586	357
3/2	1/4	932	212	1116	386	1606	530
1/4	1/2	1356	414	1112	480		
1/2	1/2	2180	1184	1350	570	1183	460
1	1/2	718	249	841	302	1219	668
3/2	1/2	1201	336	1124	460	1634	453
1/4	1	1191	322	1183	392		
1/2	1	2318	938	1387	507	1189	465
1	1	773	206	1055	300	1496	491
3/2	1	1325	244	1132	408	1657	418

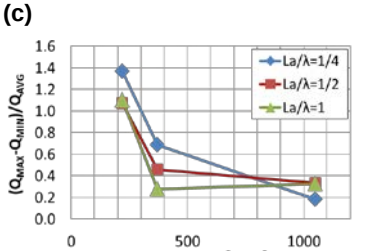

Figure 26: Experimental Results of Behavior of 324 Devices having a Fixed AlN Plate Size, Operating at 3 Different Frequencies, and having Variable Anchor Size

(a) Basic resonator geometry and parametric variations for different frequencies. (b) Table showing average Q and standard deviation (9 samples each) for resonators of different anchors width, Wa, and length, La. (c) Plot showing how Q varies largely as a function of anchor size at lower frequencies.

To determine the *Q* dependence on temperature and further investigate the sources of energy loss in the AlN CMRs we performed a test on 3 equivalent resonators working at 220 MHz and 1.05 GHz. We have chosen these resonator frequencies since they are mostly affected by two independent damping mechanisms. As it was done previously, 16 different combinations of Wa/λ and La/λ were tested. In total a sample of 96 resonators (48 for each *fr)* was measured. The experiments were performed on a cryogen-free micro-manipulated probe station (model CRX-VF Lakeshore) that allowed us to lower the temperature down to cryogenic temperature (10 K) and study the resonator response at that temperature and at room temperature (300 K).

These experiments have allowed us to validate our hypothesis of anchor losses impacting the *Q* of AlN CMRs at 220 MHz. As it is shown in Table 1, the largest (green) and smallest (red) variations of *Qu* with temperature correspond to $Wa/\lambda = 1/2$ and $Wa/\lambda = 1$, respectively. This essentially indicates that if the level of energy loss due to the anchors is small ($Wa/\lambda = 1/2$) another temperature dependent dissipation mechanism is dominant and, vice versa, this becomes negligible when the energy loss due to anchors is large ($Wa/\lambda = 1$) (in theory anchor losses should exhibit very limited temperature dependence). Secondly, when *fr* is equal to 1.05 GHz the relative variations observed for all Wa/λ and La/λ are large. This fact implies that the primary source of damping at this frequency is temperature dependent and anchors only play a secondary role.

Table 1. Average, Standard Deviation, and Relative Variation of Qu from a Sample of 3 Equivalent Resonators at 220 MHz, and 1.05 GHz at Two Temperatures: 10 and 300 K

		f_r= 220 MHz					f_r= 1 GHz				
		Q_u at 10K		Q_u at 300K		$\frac{AVG^1-AVG^2}{AVG^2}$	Q_u at 10K		Q_u at 300K		$\frac{AVG^1-AVG^2}{AVG^2}$
W_a/λ	L_a/λ	AVG^1	STD DEV	AVG^2	STD DEV		AVG^1	STD DEV	AVG^2	STD DEV	
1/4	1/4	2495	99	1871	54	0.33					
1/2	1/4	4566	1376	3132	351	0.46	4416	162	2176	419	1.03
1	1/4	725	83	694	85	0.04	5394	221	2670	173	1.02
3/2	1/4	1374	309	1174	95	0.17	5081	416	2617	110	0.94
1/4	1/2	2340	85	1730	45	0.35					
1/2	1/2	5786	2464	3288	519	0.76	4363	4	2204	1	0.98
1	1/2	881	104	859	118	0.03	4307	158	2060	249	1.09
3/2	1/2	1748	458	1528	155	0.14	4504	662	2068	523	1.18
1/4	1	1942	100	1599	78	0.21					
1/2	1	6072	492	3594	187	0.69	3817	138	2118	263	0.8
1	1	882	144	846	90	0.04	4879	368	2479	100	0.97
3/2	1	2208	258	1746	81	0.26	4914	822	2718	61	0.81

In addition, we introduced a new technique to reduce anchor losses in AlN CMRs. The technique has been applied to 220 MHz AlN CMRs and has brought an improvement of Q of almost 50%, without any deterioration of the electromechanical coupling coefficient. This approach uses etched slots in the body of the resonator (Figure 27), and close to the anchors, to limit the energy leaking to the substrate through the anchors. The slots behave as acoustic reflectors placed at the edge of the resonator's active region. These reflectors reduce the energy transmitted to the substrate, increasing the acoustic energy trapped in the cavity.

The average measured *Q* for each configuration is shown in Figure 28. This trend shows that increasing the slot's length with respect to the acoustic wavelength ($\lambda \approx 40\mu m$) results in an improvement of *Q*. Indeed, configuration D presented the highest quality factor. The measured trend is in line with the analytical prediction (Figure 28 – in green). This validates the design approach and confirms that the use of slots can improve the Q of resonators operating at 220 MHz. As shown in Figure 28, the improvement in *Q* comes with a proportional decrease of *Rm* with respect to the conventional configuration. Since this design approach does not deteriorate *kt 2*, an almost 50% improvement in the *FoM* of the resonator has been obtained. The measured admittance of the best devices for each configuration is shown in Figure 28.

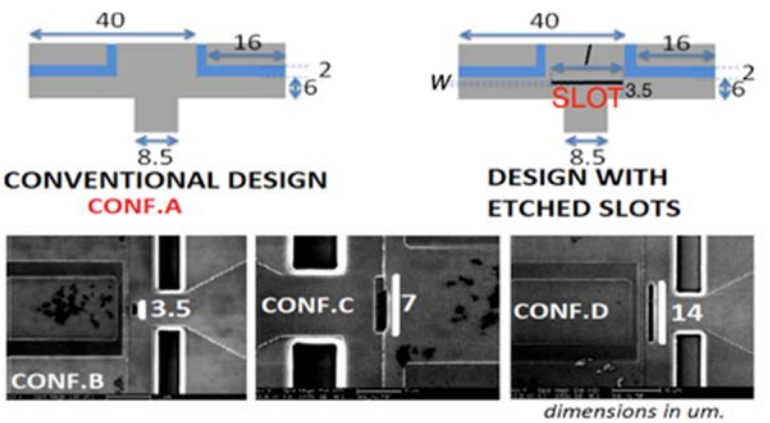

Figure 27: Example of Different Types (Conf. A ~ D) of Slots that were Introduced in the Resonator Body near the Anchor in Order to Minimize the Amount of Energy Escaping through the Supports

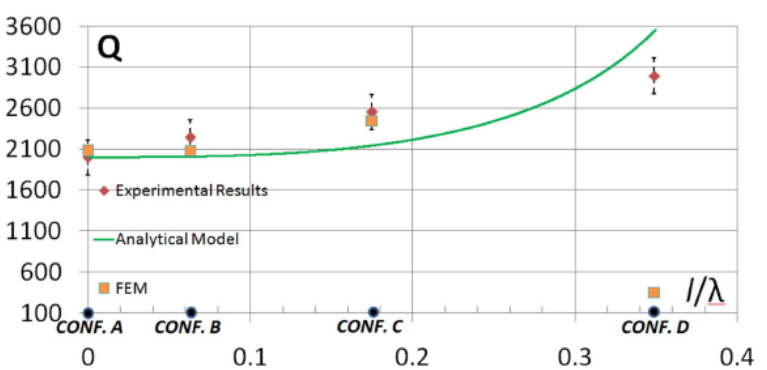

Figure 28: Red Diamonds: Experimentally Obtained Average Q for Configurations A, B, C, and D, Yellow Squares: Q Simulated by FEM, and Green Line: Analytical Prediction of Q as a Function of the Slot's Length l

2.9 Analysis of the Impact of Release area on the Resonator *Q* by Laser Doppler Vibrometery

Here we consider the effect of the motion of the substrate at the anchor attachment points on device *Q*. When modeling these devices, the assumption is usually made that the outer end of the anchor is fixed with respect to the substrate. This simplifies analysis but is not completely accurate due to the fact that an isotropic etch step is used to release the device itself from the substrate. This etch process also undercuts the region of the device layer outside of the anchor region (Figure 29). This region will undergo displacement as a result of the resonator motion. This energy leaves the body of the resonator through the anchors and is largely unrecoverable.

To determine the effects of this substrate motion, the out-of-plane displacement of a 220 MHz aluminum nitride resonator was measured using the Polytec UHF-120 Laser Doppler Vibrometer (LDV) along a path shown in Figure 29. Electrical measurements were also taken to find *Q* and k_t^2. The device then underwent a XeF_2 etch to release additional substrate area. The measurements were then taken again. This sequence was repeated eight times. We show that there is a variation in *Q* of 28% due to the effects of the released region and that this variation occurs as a function of *L*, the distance from the active region of the device to the edge of the released region of the substrate (Figure 29).

In a CMR, the primary motion is in-plane which cannot be directly measured with the LDV. Despite this, there is out-of-plane motion due to the Poisson effect and due to the piezo-electric effect. To this end, a finite element model was built which included perfectly matched layers (PMLs) to simulate this device. This model was validated by matching its out-of-plane motion with that of the LDV measurements. The energy flux through the resonator anchors produced by finite element analysis (FEA) could then be compared to the released substrate length, *L*.

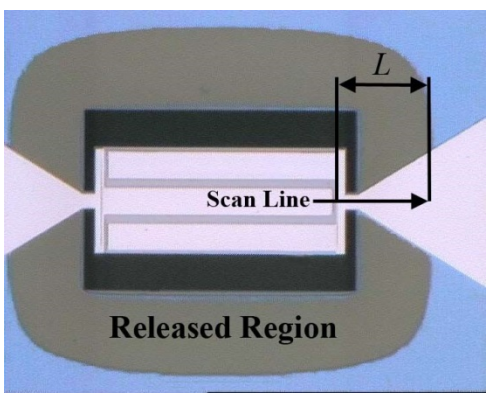

Figure 29: A 220MHz AlN CMR
The device layer immediately around the CMR has been released from the substrate and exhibits strain as the result of energy dissipated out of the anchors. The released length, L, was found to have a direct effect on device Q.

Admittance data was collected using a Rhode & Schwarz ZVL VNA. The device was probed using an Infinity probe from Cascade Microtech and the VNA was calibrated using a Cascade Microsystems impedance standard. From this data, resonant frequency, $f0$, Q, and k_t^2 were extracted.

The out-of-plane displacement measurements were taken using the LDV through a 50X objective. The spot size is approximately 2μm. The device was driven using a Rhode & Schwarz SMBV100A function generator. The device was probed in the same setup as the VNA measurements. The device was scanned along the path shown in Figure 1 with a spatial resolution of 366nm. It was driven at -6dBm and at its resonant frequency determined by the electrical measurements. This power level was chosen to prevent the resonator from operating in a nonlinear regime while still inducing enough out-of-plane motion to be detectable with the LDV. Displacement data was collected with an out-of-plane resolution of 4.2pm and with a noise floor of 4pm. The resolution bandwidth was 19.5 kHz.

A COMSOL Multiphysics model of the resonator body, anchors, and surrounding substrate was made. The geometry of the model was taken from the fabricated device, and PMLs were used to model the semi-infinite substrate. The PML layers were used at the edges of the silicon and AlN layers and on the upper electrode layer near the region of interest (shown in black in Figure 29). The PMLs were placed 300μm from the outer edge of the anchor in the direction of the scan path. This distance is far enough from the edge of the fixed substrate region so that any reflections at this interface could be taken into account in the simulations. The simulated magnitude and wavelength of the out-of-plane displacement were compared to that of the LDV measurements along the same path (Figure 29) to validate the model. The model was then simulated for each release distance, L, from the experiment and the energy flux through the outer cross-section of the anchor (Figure 30) for each release distance was calculated.

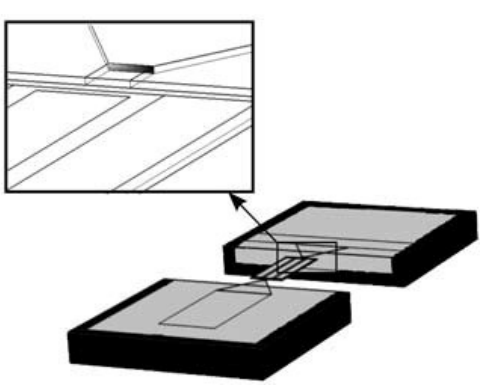

Figure 30: COMSOL was used to Measure the Energy Flux through this Cross Section in the Anchors over One Cycle

Perfectly matched layers (shown in black) were used to simulate a semi-infinite substrate.

Figure 31 shows the LDV measurements and COMSOL simulation of the displacement of the substrate region shown in Figure 30 before any additional etching. This quality of fit of the simulation to the LDV data validated the COMSOL model. To provide a value that is proportional to strain energy, the magnitude of the displacement profiles from Figure 31 were squared and then the area under the resulting curve was

integrated. This was done for each etch step and the data is plotted in Figure 32. The amount of energy released by the active region towards each anchor is a periodic function of the width of the bus bar, *d*, and the anchor length, L_a, and is governed by the equation:

$$E_{anchor} = \mathrm{abs}\left(\frac{\sin(2kD)}{4Z_0}\right) \tag{7}$$

where $D = (L_a + d)$, k is the wave number, and Z_0 is an equivalent characteristic impedance of the active region of the resonator. Equation 7 shows that the minimum energy is transmitted from the active to the inactive regions when the dimension, *D*, is a multiple of $\lambda/4$. In the current study *D* was considered to be equal to the entire released length *L* from Figure 32 and this equation was fit to the displacement data in Figure 33. When *L* is a multiple of $\lambda/4$ the inactive region acts as a $1/4\lambda$ transformer to place a virtual fixed boundary at the edge of the active region. This confines the maximum amount of acoustic energy into the active region and minimizes the energy lost to the anchor/substrate region. As shown in Figure 33, when this occurs the displacement in the anchor region increases but the corresponding ratio between the displacements in the active and inactive regions increases as well. This overall decrease in energy flux through the anchors can be seen in the FEA results in Figure 33. Minima occur at $n\lambda/4$, corresponding to the clamped condition at the edge of the anchor region.

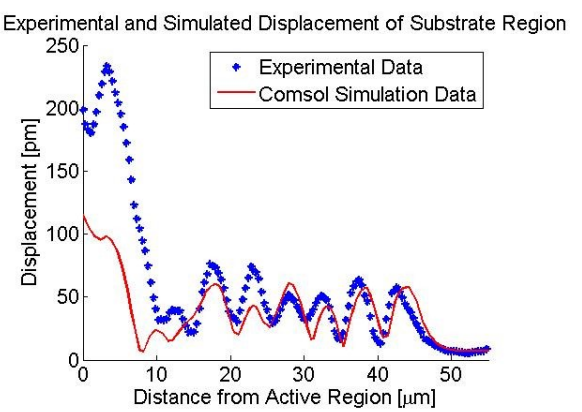

Figure 31: The Experimental and COMSOL Simulated Displacement of the Released Region of the 220MHz Resonator

The exceptional match of the simulated and LDV data validates the COMSOL model.

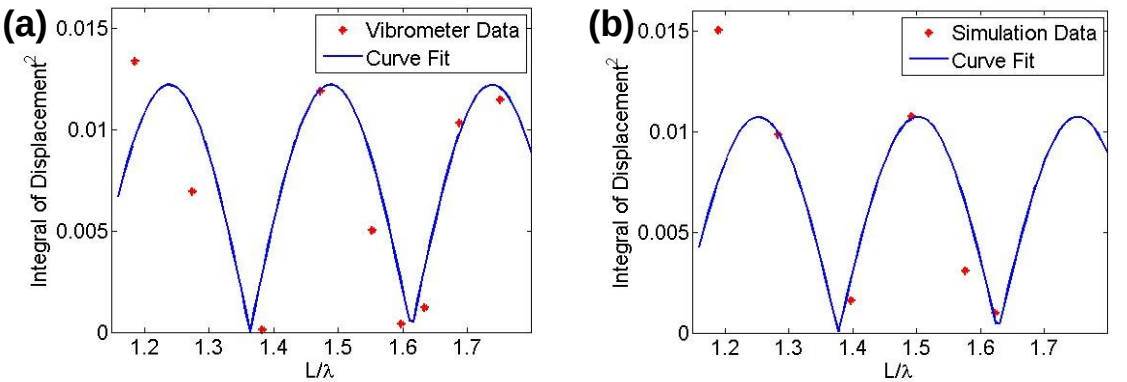

Figure 32: The Integral of the Squared Displacement of the Experimental LDV Measurements (a) and COMSOL Simulations (b) at each Etch Step and the Analytical Fits as a Function of the Wavelength, λ, from the Active Region

A maximum displacement occurs every 9.7μm, which corresponds to nλ/4.

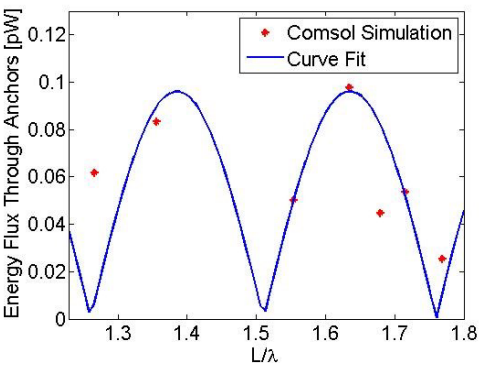

Figure 33: The Simulated Energy Flux through the Anchors of the Resonator over a Complete Cycle

A minima occurs every nλ/4. This occurs as a result of the inactive region acting as a 1/4λ transformer and placing a virtual fixed-boundary condition at the edge of the active region. This serves to contain the acoustic energy within the active region of the resonator, improving Q.

This minimization of energy loss corresponds to maxima in *Q*. Table 2 gives the values for *Q*, k_t^2, and the resonant frequency that were extracted from electrical measurements collected at each etch step. Figure 34 shows the quality factor as a function of *L*. Device *Q* varied by 28% as the released distance increased. A similar equation from was modified to account for the released area:

$$\widetilde{Q} = \frac{Q_{eff}}{1 + 2\alpha\left(\frac{2abs(sin(2kL))}{4Z_0}\right)} \tag{8}$$

where Q_{eff} is the ideal *Q* with no anchor loss, and α is proportional to the amount of energy lost to the anchor from the active region of the resonator. An identical $\lambda/4$ variation can be seen for *Q* with peaks at $n\lambda/4$.The k_t^2 values for each etch step varied by approximately 11% but did not follow any trend as Q did. Since the

measured device k_t^2 was independent of L, we can confirm that the out-of-plane motion in the inactive region must vary proportionally to Q due to conservation of energy. This fact explains the same periodicity of displacement and Q with respect to L.

Table 2. The Released Distance, L, Q, k_t^2, and Resonance Frequency for each Release Step

L [μm]	Q	$k_t 2$	f_0 [MHz]
46.15	1866	.3949	218.86
49.81	1631	.3943	218.85
54.21	1517	.4148	218.76
57.88	1897	.4056	218.43
61.17	1621	.3858	218.58
63.0	1403	.3760	218.35
64.5	1419	.4156	218.36
66.7	1676	.4255	218.37
69.2	1951	.4140	218.57

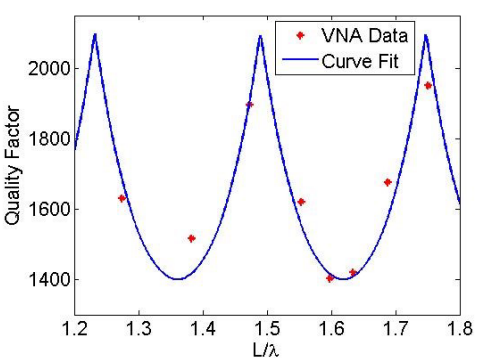

Figure 34: The Quality Factor at each Etch Step
Q varies by 28% as the etch distance is increased. The maxima at nλ/4 correspond to points of minimum energy loss through the anchors.

2.10 Thermoelastic Damping in AlN CMRs

This work experimentally verifies that the main intrinsic material damping in laterally-vibrating composite piezoelectric resonators is of thermodynamic nature and concludes that it comes primarily from TED in the metals that are used to sandwich the piezoelectric film. The Qs of 1GHz resonators formed by AlN sandwiched between Pt and 3 different kinds of electrode metals were measured from cryogenic (50K) to room temperature. The trends exhibited by Q vs. temperature for different electrode materials find very good agreement with the theory of TED in metals. This study helps clarifying the debate about what the dominant damping mechanism is in this class of RF MEMS transducers when anchor losses are mitigated.

Previous work on laterally-vibrating (symmetric Lamb mode) composite piezoelectric resonators has demonstrated that a damping mechanism of thermodynamic nature is dominant at ultra-high frequencies (UHFs) and when anchor losses are reduced by properly designing the supports at lower resonance frequencies (ω_r). Several claims have been made about the origin of intrinsic material damping in this class of MEMS transducers: stress or velocity jump across the metal-piezoelectric interfaces, TED in the electrodes, charge redistribution due to the mode of vibration. In this paper, we confirm through experiments that the TED model can accurately describe the trends of *Q* vs. temperature reported for 1GHz AlN resonators with different electrode metals over the temperature range of study.

We hypothesize that damping in 1GHz resonators formed by an AlN thin film sandwiched between metals is mainly due to TED in the electrodes. According to this model, metallic structures behave as anelastic solids when they are subjected to stress and the intrinsic damping (Q_{ted}^{-1}) is set by both relaxation strength ($\Delta_M=(\varepsilon_R-\varepsilon_U)/\varepsilon_R$) and time ($\tau$) constants (Figure 35) and exhibits a Lorentzian behavior with $\omega_r\tau$. Assuming $\omega_r\tau<<1$ for most metals [8], Q_{ted}^{-1} can be expressed as a function of the intrinsic material properties of the electrodes and, in particular, of the thermal properties that show the largest variations with temperature.

$$Q_{ted}^{-1} = \Delta_M \frac{\omega\tau}{\omega^2\tau^2+1} \propto \frac{\beta^2\kappa T}{C_p^2} \tag{9}$$

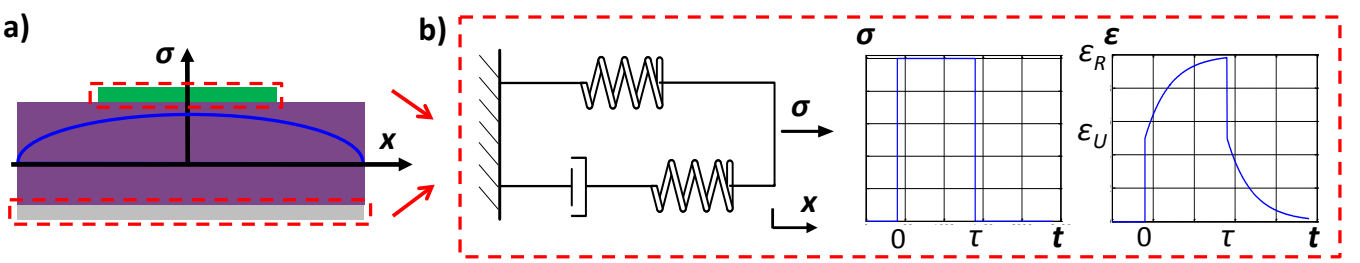

Figure 35: (a) Schematic View of the Cross Section of One-Finger Laterally-Vibrating Composite Piezoelectric Resonator and (b) Equivalent Mechanical Model of the Metal Layers and Time Responses of the Resulting Strain (ε)

(a) consists of two metal layers (bottom plate and top electrodes) and one piezoelectric film subjected to uniaxial stress (σ) and (b) time responses of the resulting strain (ε) given the applied σ under the assumption of standard anelasticity. ε_U and ε_R are respectively the unrelaxed and relaxed ε and τ is the relaxation time.

To corroborate our hypothesis we measure and fit through Eq. (9) the Q^{-1} for AlN resonators (a total sample of 15 devices) having 3 different electrode metals (Pt, Au, and Al), hence different thermal properties (Table 3), at a temperature range of 50 to 300K. To collect statistics and exclude the impact of process variations 5 identical devices built on the same wafer were tested for each metal. Each resonator is formed by a rectangular AlN plate (1.1μm-thick) sandwiched between a Pt bottom plate (100nm-thick) and a top electrode layer (100nm-thick) and fabricated.

Table 4 shows the average electromechanical coupling (k_t^2) and Q, whose product constitutes the device figure of merit (FoM), and estimated series resistance (R_S) of each resonator under test. To exclude the impact of electrical loading we compare the unloaded Qs (Q_u) of the resonators, which are extracted from the loaded Qs (Q_l) as shown in [1]. Figure 36 plots both experimental and theoretical $1/Q_u$ for different temperatures. The theoretical values are obtained using Eq. (9) and adding the impact of anchor losses, which is computed by means of finite element method (FEM) techniques (Q_{anc}=9000). As there are 2 metal-to-AlN interfaces in the resonator under study, we calibrated the impact of Pt on Q_{ted} by fitting the Pt-AlN-Pt data to our model and determining the proportionality factor that corresponds to Pt in Eq. (9). In general, the plots show similar trends for both experimental and theoretical data, which validate our hypothesis of TED being the main source of damping in this class of piezoelectric MEMS resonators.

Table 3. Summary of Electrical and Thermal Properties of the Metals under Study at Different Temperatures

The resistivity (ρ_e) and thermal conductivity (κ) correspond to the actual thin film values measured and derived through the Wiedemann-Franz law, respectively. Instead, the rest of the coefficients (thermal expansion (β) and specific heat (C_p)) correspond to bulk values.

	ρ_e [Ωnm]			κ [W/mK]			β [ppmK^{-1}]			C_p [J/KgK]		
T [K]	Au	Pt	Al	Au	Pt	Al	Au	Pt	Al	Au	Pt	Al
50	28.6	81.5	32.9	256	90	223	8	3.7	3.7	73	55	210
100	32.2	105	34.9	227	69.4	210	12	6.7	12.2	109	100	600
150	34.2	125	37.6	214	58.3	195	13	7.9	17.2	120	117	800
200	36	146	39.5	203	50.2	185	14	8.4	20	124	125	850
250	45.1	168	44.6	162	43.6	164	15	8.7	21.8	127	130	900
300	57.9	190	63.4	126	38.5	115	15	8.9	23	129	133	900

Table 4. Summary of the Experimental Data Collected for a Sample of 15 25-finger 1 GHz Laterally-Vibrating AlN Resonators

The average values are calculated over 5 repetitions of the same device.

	Pt-AlN-Pt				Au-AlN-Pt				Al-AlN-Pt			
T [K]	k_t^2 [%]	Q_l	R_S [Ω]	Q_u	k_t^2 [%]	Q_l	R_S [Ω]	Q_u	k_t^2 [%]	Q_l	R_S [Ω]	Q_u
50	1.49	2773	11.22	5111	1.27	3232	4.05	3873	1.50	5074	4.40	7564
100	1.49	2411	14.12	4752	1.27	2832	4.07	3343	1.48	4665	4.36	6644
150	1.54	2010	16.13	3900	1.25	2598	4.46	3046	1.49	3961	4.70	5498
200	1.46	1785	18.91	3522	1.26	2274	4.75	2636	1.43	3490	5.07	4746
250	1.43	1598	21.94	3250	1.24	2109	6.15	2522	1.53	3117	6.24	4386
300	1.75	1374	26.35	3247	1.27	2007	8.43	2540	1.60	2693	8.91	4181

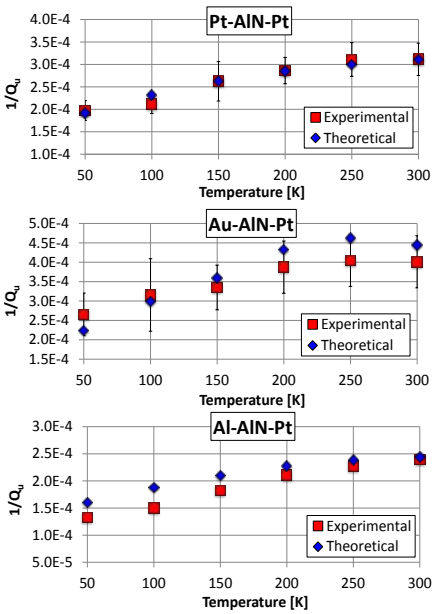

Figure 36: Evolution of Experimental and Analytical Q^{-1} Assuming TED versus Temperature for 25-finger 1 GHz AlN Resonators having as Top Electrode Metals either Pt, Au, or Al

2.11 Resonator Ovenization

We have designed and demonstrated an integrated oven for AlN piezoelectric MEMS resonators (Figure 37) that enables device heating from -40°C to +85°C with a power consumption as low as 368μW – the lowest ever recorded for MEMS resonators. The same resonators exhibit quality factors (*Q*) as high as 4,459. In this work, RF power delivery is decoupled from resonator supporting beams, hence alleviating the trade-off between power consumption and *Q*-factor; moreover, heaters are placed externally to the resonator body, hence eliminating the deleterious effects of serpentines on the acoustic properties of the device. More importantly, this ovenization technique is independent of the resonator geometry, so it is broadly applicable to any resonator frequency (70 MHz to 1.16 GHz in this work). This demonstration constitutes a fundamental stepping stone in enabling temperature stable oscillators with extremely low power consumption.

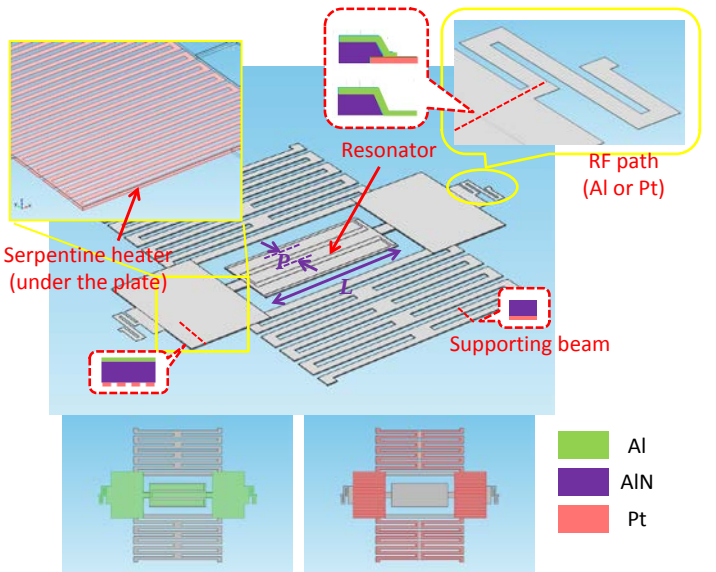

Figure 37: Schematic Representation of a Low Power Ovenized Resonator
Supporting beams are composed of AlN and Pt while the RF paths are composed of only a thin metal layer (AlN is completely removed). Pt serpentine heaters are placed under the rectangular plates. DC routing and RF routing (shown in the insets at the bottom) are orthogonal and separated by AlN layer where they cross (i.e. RF routing occurs in the top metal layer, whereas DC routing is done through the bottom metal layer). L and P are the length and pitch of the resonator body, respectively.

Oven-controlled MEMS resonators are promising candidates for high precision oscillators and are superior to oven-controlled crystal oscillators (OCXOs) in terms of power consumption. Research activities on ovenized MEMS resonators have shown that device heating from -40°C to +85°C requires only mW of power. To enable the use of miniaturized frequency sources in truly disruptive applications such as in sensor nodes, pico-satellites or unmanned nano-air vehicles, sub-mW power consumption is required. The work presented herein sets a new record for minimum power consumed to ovenize MEMS resonators.

Ovenization power under high vacuum is set by the thermal resistance of the suspensions that connect the resonator to the substrate. Conceptually, low power ovenization is attained by decoupling RF power delivery from the resonator supporting beams. By engineering the geometry of the mechanical suspensions (designed to be long but stiff) and electrical routing (from which high thermal conductivity AlN was removed) it is possible to attain a total thermal resistance ($R_{beams}||R_{RF\ paths}$ in Figure 38) > 10^5 K/W. Various designs were evaluated analytically and via COMSOL FEA (see Figure 39). The analysis also took into account the impact of air conduction and convection at different pressure levels.

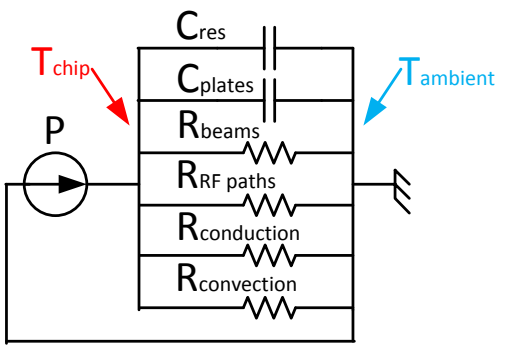

Figure 38: Schematic Representation of Thermal Equivalent Circuit
$R_{beams}||R_{RF\ paths}$ represents the total thermal resistance of solid materials connected to the substrate.

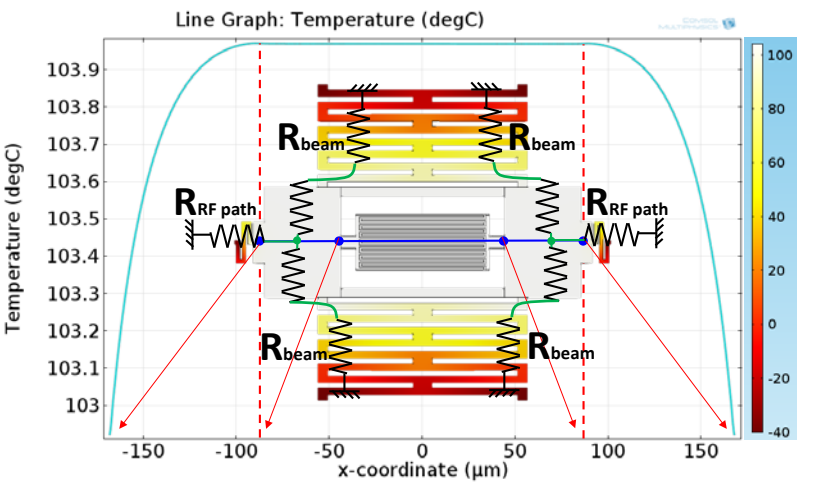

Figure 39: COMSOL FEA of Temperature Distribution in one of the Devices of this Work given a Fixed Voltage is applied to the Heater
There is no temperature gradient across the resonator.

It is important to note that two heaters are placed symmetrically under two rectangular plates connected to the central body of the resonator. This symmetric configuration ensures that the resonator is uniformly heated and does not see any temperature gradient (Figure 39). Furthermore, the separation of the heater from the body of the resonator facilitates achieving high Q and k_t^2. The resonator is effectively unchanged with respect to its standalone configuration (without heater) and does not experience any of the topography introduced by a heater that sits right under it. The ovenized resonators can be manufactured in the same process used for conventional devices without requiring any additional step (Figure 40).

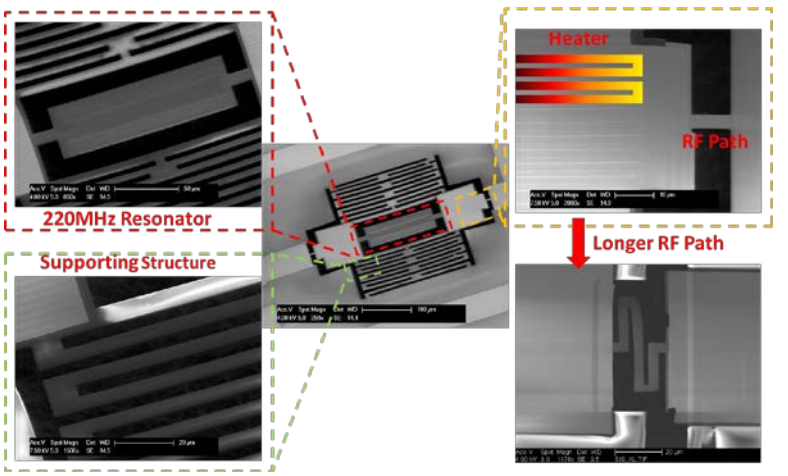

Figure 40: SEM Pictures of a Fabricated Low Power Ovenized AlN Resonators
Insets show zoomed-in views of the resonator, supporting structure, and 2 different RF paths.

Under high vacuum (~1e-8Torr), the maximum power required to change the resonators' temperature from -40°C to +85°C is about 10X smaller than what is required to ovenize a resonator having the heater integrated in the body of the device. The power consumption is extracted from the separate measurement of the resonator frequency change per applied heater power and the temperature coefficient of frequency (TCF) of the resonator (Figure 41-42). Such ovenization method is universally suitable for both low and high frequencies. Interestingly, and as expected, the resonators show high Q and k_t^2 (Table 5).

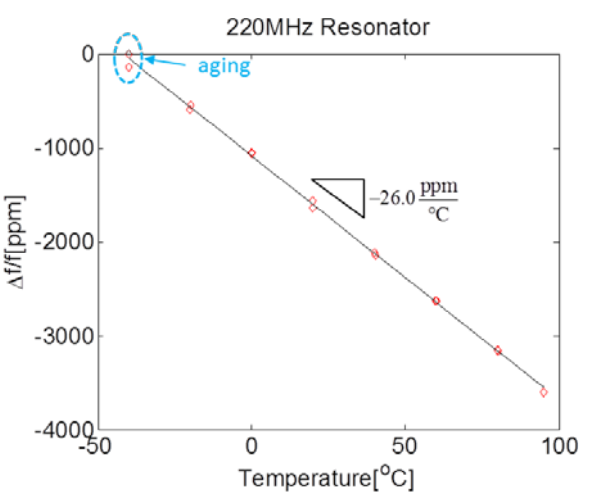

Figure 41: Measured Frequency Shift versus Temperature in a Lakeshore Vacuum Probe Station for a 220MHz Resonator

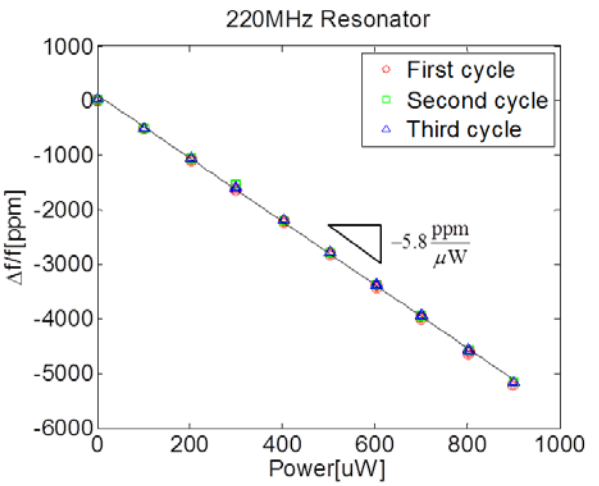

Figure 42: Measured Frequency Shift versus Applied Power in a Lakeshore Vacuum Probe Station for a 220MHz Resonator

Table 5. Performance of Low Power Ovenized Resonators

Frequency [MHz]	Q	k_t^2 [%]	Temperature Rise Factor [°C/mW]	Extracted Max. Power [μW]
70	2774	1.02	224	559
220	4459	0.54	223	560
550	3959	1.03	278	449
1160	1247	1.08	340	368

It is important to note that heat convection and conduction through air cannot be neglected for the ovenized resonators, as they occupy a relatively large surface area. Table 6 shows the dependence of power consumption on pressure. It also shows that 30mTorr (a typical pressure for wafer level packaging) is low enough to attain sub-mW power consumption.

Table 6. Power Consumption of 70MHz Resonator versus Pressure

Pressure [Torr]	Freq. Drift [ppm/μW]	Temperature Rise Factor [°C/mW]	Maximum Power [μW]
5×10^{-1}	-2.13	79	1576
3×10^{-2}	-5.29	197	634
8.5×10^{-6}	-5.90	220	569
$\sim1\times10^{-8}$	-5.97	224	559

We have also designed and demonstrated an elegant temperature compensation circuit based on the above sub-mW ovenized resonators. We were able to achieve 100 ppm frequency instability over a temperature range of -35-85°C with a total power consumption of 3.798mW. Compared to the state-of-the-art, this temperature compensation technology offers a simpler and more power efficient method than the previously reported oven-based temperature compensation techniques.

The temperature compensation circuit is comprised of two parts: a modified Wheatstone bridge with a dummy chip resistor and a differential resistor-capacitor (RC) integrator, as shown in Figure 43.

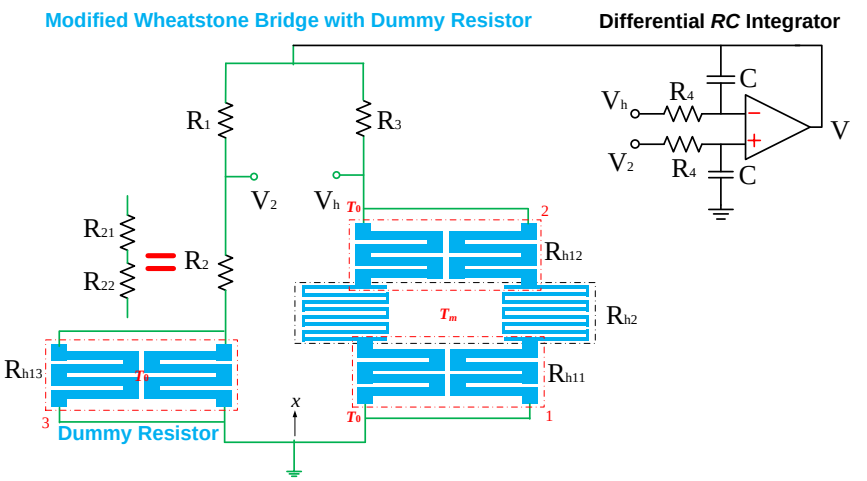

Figure 43: Schematic Representation of Temperature Compensation Circuit

In the modified Wheatstone bridge, $R_{1\text{-}3}$ are external constant resistor with R_1 equal to R_2, while R_h (=R_{h11}+ R_{h12}+ R_{h2}) is the total heater resistance. R_{h11} and R_{h12} represent the parts of resistance under the supporting beams. R_{h13} is a chip resistor which has the same geometry as R_{h11} or R_{h12}. The constant resistor can be seen as the sum of two constant resistors, R_{21} and R_{22}, which are set to be equal to R_{h11} and R_{h2} at T_m, respectively. In this case, R_{22} works as the temperature-reference resistor. By assuming a linear temperature distribution along the supporting beams, the following equation is valid for any ambient temperature T_0:

$$R_{h11} + R_{h12} = R_{h13} + R_{21} \tag{10}$$

This equation forces R_{h2} to be equal to R_{22} (set to be equal to R_{h2} at T_m). Since there is little temperate gradient in the rectangular plates where the heaters reside, the plate temperature is kept at T_m and so is the resonator. Figure 44 shows the experiment results of resonator frequency responses with respect to the ambient temperature changes before and after temperature compensation.

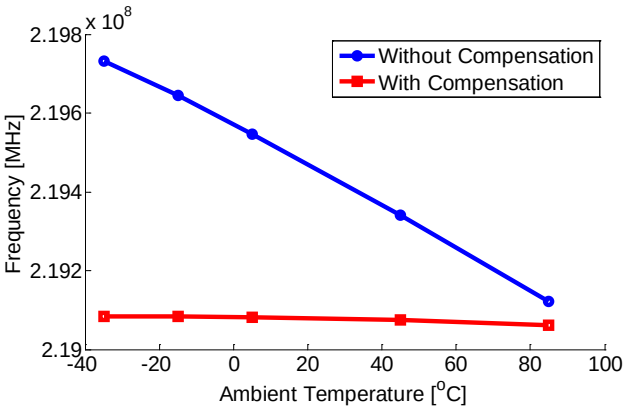

Figure 44: Plots of Resonator Frequency Responses with Respect to the Ambient Temperature Changes before and after Temperature Compensation

2.12 Temperature Compensation Circuit

2.12.1 Colpitts Oscillator with AlN Contour Mode Resonator

At the beginning phase of the project, the conventional differential Colpitts oscillator was designed by IBM 130nm tech and an AlN CMR was used for the frequency selective element. Figure 45 shows a microscopic image of the oscillator package and the test environment representing how the output signal was measured respectively. The oscillator works from a 0.9 V power supply and its center frequency is 1.16GHz with 10 dBm RF output power.

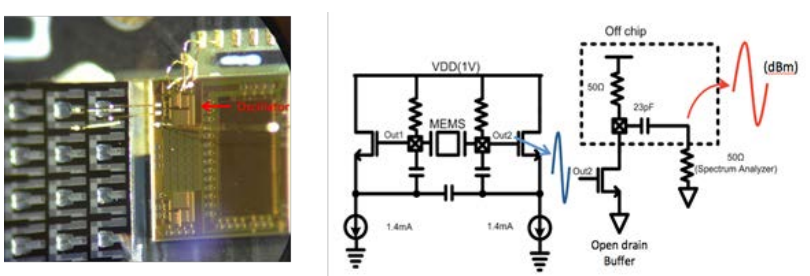

Figure 45: Die Photo of the Oscillator and AlN Contour Mode Resonator (left) and Test Environment (right)

To test the phase noise of this oscillator, the noise floor inherent in the test equipment (Agilent Technology E5052B) should be considered. Figure 46 shows the measured phase noise result of the oscillator (line) along with the noise floor of the test setup (dot). At around 1 MHz offset frequency, there was a dip in the phase noise response. This feature is consistent with the difference in fs and f_p (roughly 1 MHz); this dip in phase noise was due to a reduction in tank impedance at f_s.

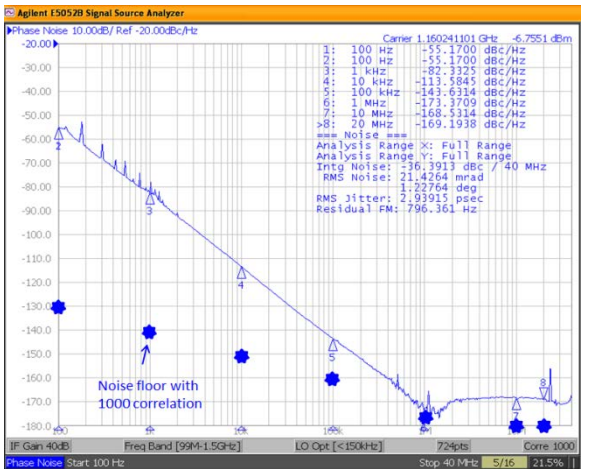

Figure 46: Phase Noise Measurement

This chip exploited intrinsically high *Q*s of AlN CMRs to achieve good phase noise performance. The phase noise at 1 MHz offset frequency was -173.3 dBc/Hz. The measured jitter (integrated from 12 kHz to 40 MHz) was 2.9 ps rms, as shown in Table 7. This test result is based on the AlN CMR device fabricated in Phase II. Devices from Phase III had parasitic capacitances between the sensor and the heater, which are unavoidable due to its structure. Figure 47 shows the layout of AlN CMR and indicate which spots contribute to such undesirable capacitance. Due to the parasitic capacitances, the power consumption is larger and phase noise performance is higher compared to the simulation result.

Table 7. Phase Noise of the Oscillator at each Offset Frequency

Offset(Hz)	**1k**	**10k**	**100k**	**1M**
PN(dBc/Hz)	-82.3	-113.5	-143.7	-173

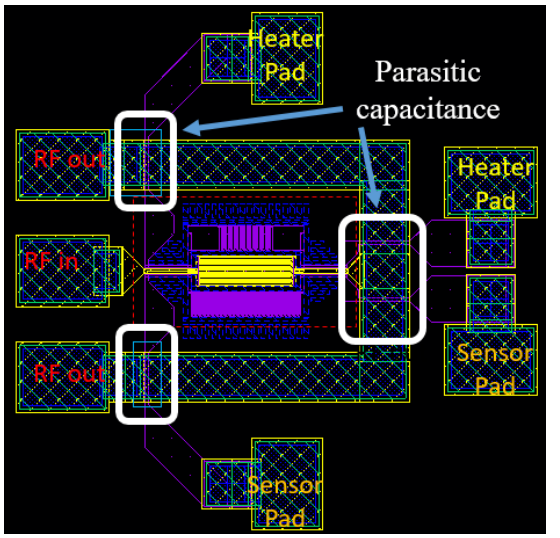

Figure 47: Layout of the AlN CMR with Specific Area Contributing Parasitic Capacitance

Figure 48 shows the admittance of a resonator as a function of frequency. Here, a resonator has two parallel frequencies at which oscillator can work. For example, an oscillator can be tuned to work at spurious 2 modes. Since the impedance of this point is smaller than spurious 1 mode, it requires more power consumption than when the oscillator works at spurious 1 mode.

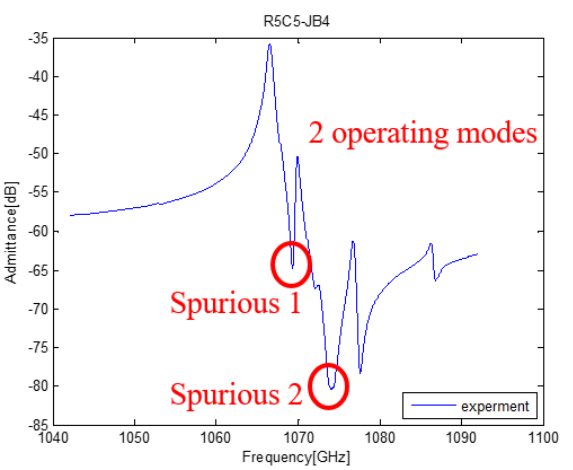

Figure 48: Admittance of an AlN CMR according to Frequency Change

The quality factors of two modes are also different from each other, and consequently, the measured phase noise is different even though the same type of Colpitts oscillator is used. Figure 49 represents two phase noise when oscillator works at spurious 1 or spurious 2 point. Similarly, Figure 50 shows the phase noise measurement of a different CMR integrated to Colpitts oscillator. The measured phase noise of -121.6 dBc/Hz at 1 kHz offset is the best noise performance ever demonstrated from an oscillator with AlN CMR.

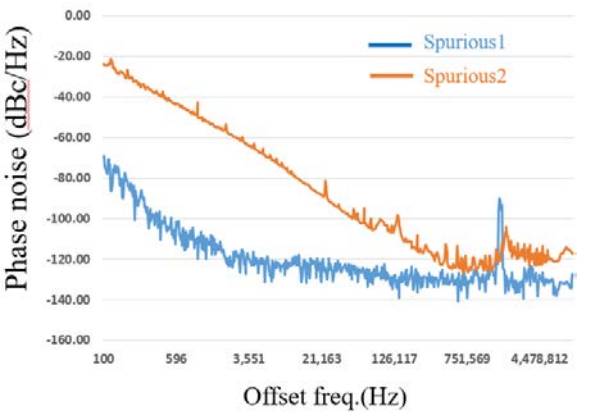

	100Hz	1kHz	10kHz	100kHz	1MHz
Spurious1 (dBc/Hz)	-69.5	-109.5	-117	-120.7	-120
Spurious2 (dBc/Hz)	-23.7	-42.7	-76.5	-103	-123

Figure 49: Two Phase Noise Performance at Different Modes (Device R5C3_JB1)

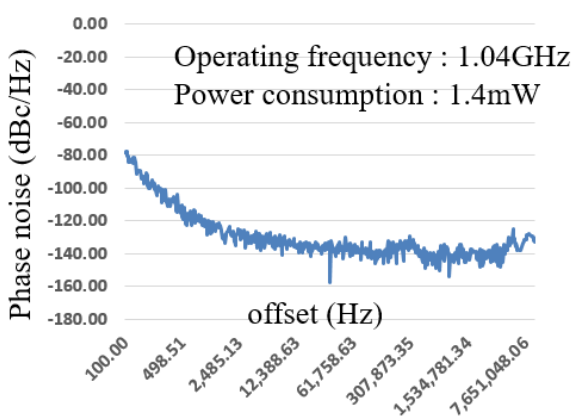

	100Hz	1kHz	10kHz	100kHz	1MHz
PN (dBc/Hz)	-78	-121.6	-133.8	-137	-144

Figure 50: Phase Noise Performance of a Different Device (Device R5C3_JB4)

2.12.2 Current Source for Temperature Compensation

The dominant source of the resonance frequency drift over temperature variation is the resonator itself (-22 ppm/°C). For crystal oscillators, temperature compensated crystal oscillators (TCXOs) and OCXOs are often employed. In contrast, this work was targeted at a microscale heater contained in the resonator itself. This heater reduces the temperature drift from the resonator to 2 ppm. However, to achieve less than 2 ppm frequency variation, the optimal design of a complementary metal-oxide semiconductor (CMOS) circuit

should be considered since the heater does not stabilize the temperature of the oscillator. Figure 51 shows the frequency variation, when the temperature coefficient of current source is zero and an ideal resonator (no temperature dependent) is used; revealing the inherent frequency drift due to temperature resulting from the CMOS circuitry.

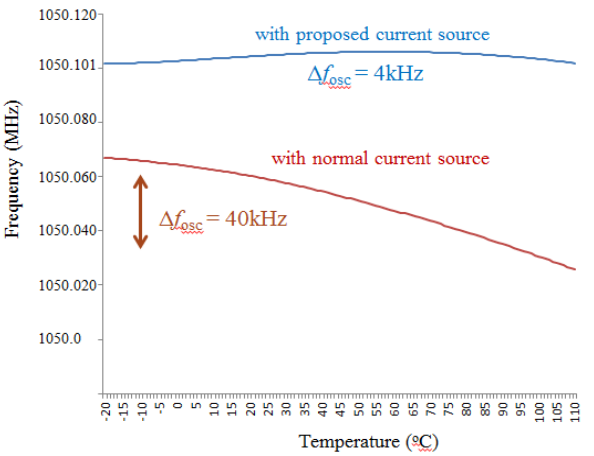

Figure 51: Simulation Result of Resonance Frequency Variation with and without Proposed Current Source

To reduce the frequency drift due to CMOS, we designed a current source that compensates for the temperature drift of the oscillator. The addition-based current source is a good candidate to stabilize oscillator frequency variation due to the CMOS temperature coefficient. Though its aim was for compensating bias current variation caused by process variation, we can modify the structure to allow temperature compensation. The proposed technique allows us to tune the temperature coefficient of the current reference to cancel residual frequency drift.

Figure 52 (a) is a block diagram of the proposed current source to compensate the frequency variation caused by oscillator. The two poly bias resistors (R1 and R2) are identical in value and layout. The resistance variation dominates the temperature coefficient of the current reference. The resistors have a positive temperature coefficient, leading to a decrease in current in M2 as temperature increases. Conversely, the current through M1 increases, allowing cancellation and tuning of the current temperature coefficient. Figure 52 (b) and (c) shows these behaviors. The simulated frequency drift of the oscillator, assuming the resonator temperature is completely stabilized and current source has zero temperature coefficient is 40 kHz (simulated). With this proposed current source having total bias current with a positive temperature coefficient, the oscillation frequency variation is decreased to less than 4 kHz (simulated). To verify this effectiveness, the test bench is set up as shown in Figure 53.

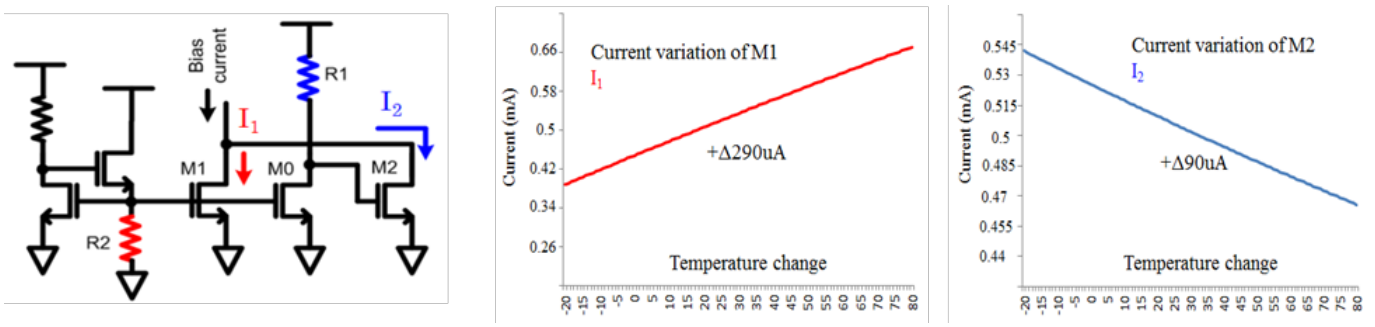

(a) **(b)** **(c)**

Figure 52: (a) Proposed Current Source and the Current Variation of (b) M1 and (c) M2 under the Temperature Change (Simulation)

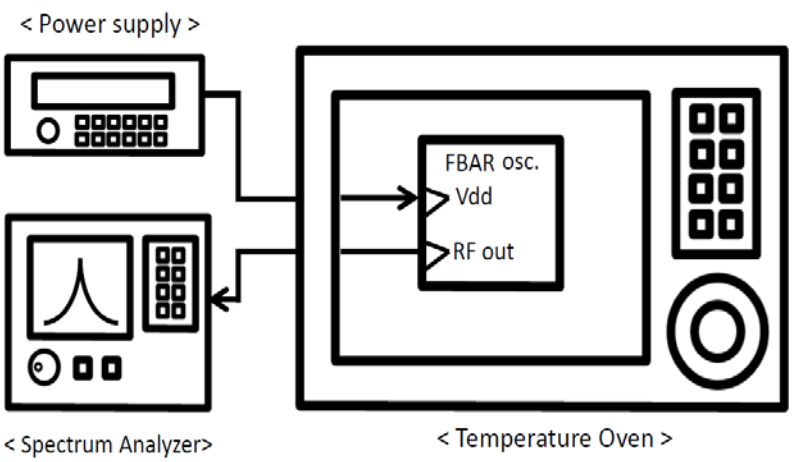

Figure 53: Test Bench for the Temperature Compensated Current Source

As the temperature was swept from 0 ^{o}C to 80 ^{o}C, the total frequency change was -1777 ppm which was equal to 22ppm/^{o}C when the temperature compensating function was off. But, when the modified current source was on, the total frequency variation was decreased by 25 kHz over the whole temperature range, which meant the frequency variation caused by oscillator decreased. Of course, the temperature variation due to the resonator remained. However, as mentioned above, using an ovenized resonator should allow us to get expected temperature coefficients around 1 ppm. Figure 54 shows the test result of a current variation with and without this current source, demonstrating the ability to tune the current temperature coefficient. Next step is for building up the system to compensate any frequency drift of the oscillator caused by resonator. The above work was effective only for CMOS circuit based frequency change over temperature. We assumed that resonator has zero temperature coefficient at the above work.

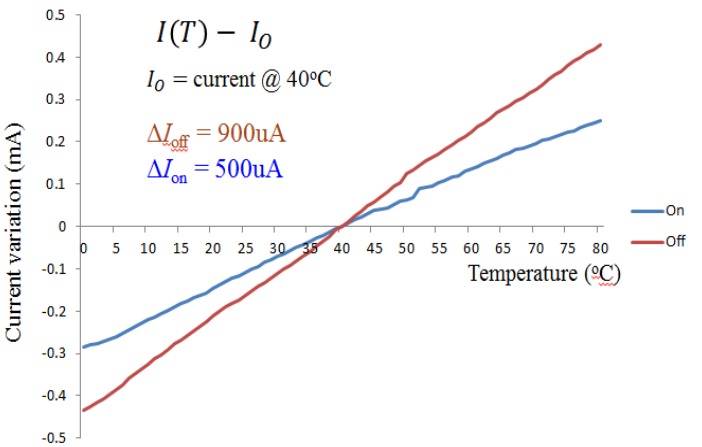

Figure 54: Test Result for the Temperature Compensated Current Source

2.12.3 Heater and Sensor

To implement the on-chip oven controlled temperature compensated system, the two essential factors are heater and sensor. Figure 55 shows how the film bulk acoustic resonator (FBAR) has a sensor and a heater integrated in the same chip with piezoelectric material. The sensor is fabricated next to top electrodes, otherwise the heater is deployed beneath the AlN layer, which minimizes the heat loss through air convection. The resistance of heater is 100ohm with a 2kohm sensor. Since the heater resistance is small, more current is needed to generate the same amount of heat compared to the AlN CMR heater which has higher resistance.

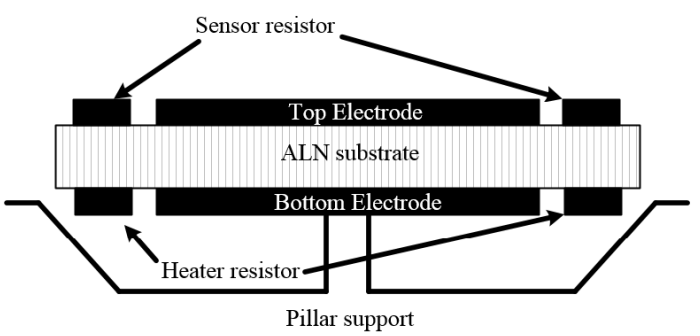

Figure 55: Block Diagram of the FBAR with Sensor and Heater

In the case of AlN CMR device, as shown at Figure 56, the heater and sensor are integrated at the side of the resonator. Here the heater resistance is 1.2kohm. Although this high resistance helps to generate the same amount of heat with smaller current, the voltage drop across the heater limits the maximum current which current steering digital-to-analog converter (DAC) can produce.

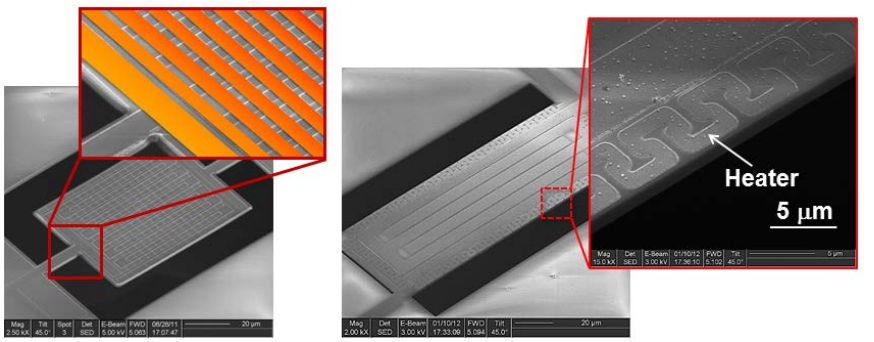

Figure 56: SEM Photo for Sensor and Heater for AlN CMR

2.12.4 Transformer Coupled Colpitts Oscillator

There have been many efforts and researches to decrease phase noise with low cost, especially for close-in offset. That's because close-in phase noise is an important performance metric for a reference oscillator, as it dominates the in-band phase noise of a frequency synthesizer in a radio. Besides using MEMS resonators, there have been many other techniques from the circuit design perspective, wherein a large capacitor was placed parallel to the current source in order to minimize its thermal noise around second harmonic of the oscillation. It is very simple to implement, but, there are trade-off between area due to a huge capacitor and noise filtering.

Another technique was introduced to reduce amplitude modulation to phase modulation (AM-PM) arising from non-linear device parasitics by using compensation capacitor. However, parasitic capacitance, one of the major factors for AM-PM conversion can vary according to the size of the current source and process variation. It was also dependents on the amplitude of the output signal and current source.

The proposed oscillator therefore removes the current source of the oscillator, which is the main source of the up-converted thermal noise. The current source is necessary for high impedance to stop the differential-pair field-effect transistors (FETs) in triode from loading the resonator in the LC oscillator. It is also helpful for Colpitts oscillator to obtain enough loop gain. The removal of the high impedance current source is compensated by using transformer and cross coupled capacitor to increase the loop gain and kick off the oscillation in this work. The proposed transformer coupled Colpitts oscillator, therefore, utilizes the benefits of conventional oscillator such as class C, D, and Colpitts to decrease the close-in phase noise as well as power consumption.

Figure 57 shows the detail block diagram with the transformer where the turn ratio between primary and secondary inductor is 2 to 1. There are two reasons to choose 2:1 turn ratio. One is to increase the feedback loop gain to double, and the other reason is to utilize the secondary inductor as a balun. Since the center tap of the secondary inductor is connected to ground, the half of the inductor is used to feed the oscillator output directly to the gate of the Quasi-passive mixer. If the signal across the FBAR is used for an output, buffer is essential which leads to more power consumption added. One of the capacitor (C_2) in the feedback loop and one secondary inductor (L_{s1}) constitute LC tank and have high impedance at their resonance frequency equivalent to operating frequency of the oscillator (w_o).

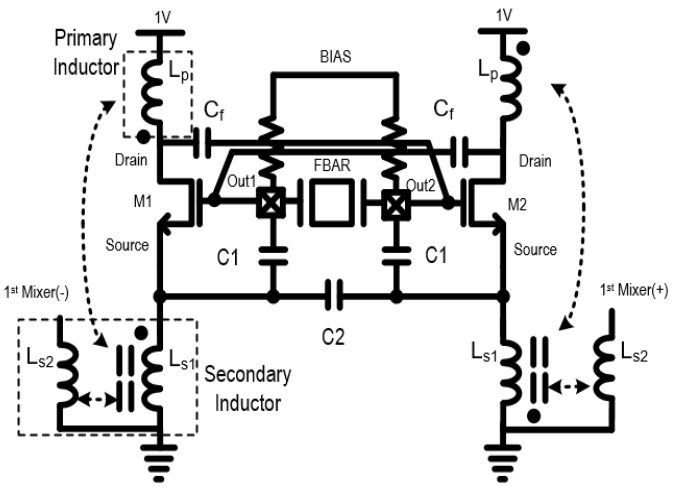

Figure 57: Block Diagram of the Transformer Coupled Colpitts Oscillator

2.12.5 Transformer Design

The Taiwan Semiconductor Manufacturing Company (TSMC) p-cell libraries offer a variety of passives, including inductors, capacitors and diodes. However, it does not have transformers. Therefore, it should be custom-made. The key parameters to design for are self-inductance (L), quality factor (Q), and the coupling coefficient (k) given area constraints. Maximizing k results in higher effective inductance per area and reduces signal loss when magnetically coupled from the primary to the secondary coil. There are two main transformer topologies: planner and stacked structure as shown in Figure 58.

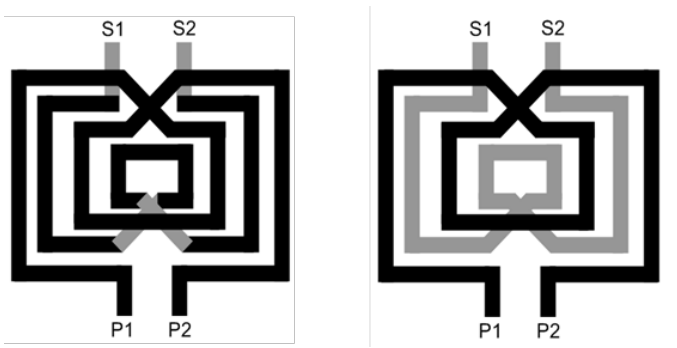

Figure 58: Planner (left) and Stacked Transformer Structure (right)

Planar structure where both the primary and secondary coils are drawn on the same metal layer, has medium Q, k, but large area. Conversely, stacked structure consisted of two metal layers, exhibits high k, L, but low Q. Based on the oscillator design, Q is a critical parameter for achieving low phase noise and lower power consumption. In TSMC library options, there is only one thick metal layer (M9) with low sheet resistance (0.005 Ω/sq). The next thickest metals (M8) has 4× higher sheet resistance, resulting in 4× lower Q. That's why the planar structure is used for this oscillator design. The planar structure almost comprises of Metal 9

(Black line). Metal 8 (Gray line) is only used for intersection part. However, the stacked transformer uses Metal 8 for secondary inductor, which leads to higher resistance and lower Q. As the proposed oscillator needs higher Q of the transformer to obtain enough loop gain and lower phase noise, planar structure is decided to be used.

2.12.6 Test Result of the Transformer Coupled Colpitts Oscillator

The oscillator is fabricated by using 65nm TSMC technology. Figure 59 shows the die photo with 2GHz FBAR device instead of AlN contour mode because of spurious modes. The transformer coupled Colpitts oscillator has a dimension of 900um by 400um. As you can see, most of the area is taken by the transformer. The power supply used for oscillation is 1V. The oscillator can start at 200uW power consumption but 350uW is needed to have a large amplitude enough to measure the phase noise.

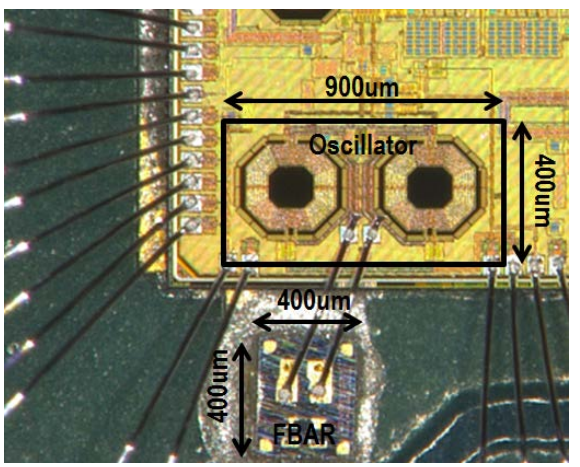

Figure 59: Die Photo of the Transformer Coupled Colpitts Oscillator

Figure 60 shows the measured phase noise. The phase noise measured from conventional Colpitts oscillator is used in the same plot for the purpose of comparison. You can see that the overall phase noise is improved. More specifically, at the close-in offset frequency, the slope decreases from $1/f^3$ to $1/f^2$.

Based on the noise profile of the oscillator that uses the MEMS resonator, the close-in phase noise up to 10 kHz offset frequency is mainly dominated by 1/f noise conversion. The parallel impedance of the MEMS resonator (R_p) and oscillator's noise factor *F* affects up to 1MHz offset frequency. Noise factor expressed by the below equation has three noise contributions, the tank resistance, the active devices and the current source respectively.

$$F = 1 + \frac{4\gamma IR}{\pi V_O} + \gamma \frac{4}{9} g_{m,bias} R \tag{11}$$

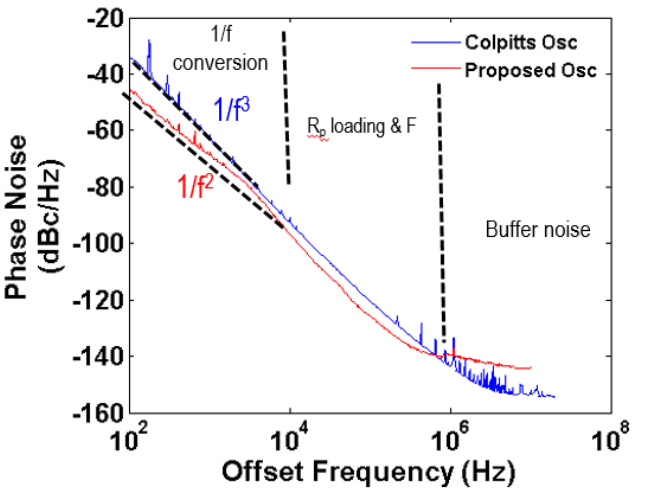

Figure 60: Measured Phase Noise Performance with Colpitts Oscillator

Since active devices should be used for generating the equivalent negative resistance needed to sustain a steady-state oscillation, the first two terms are inevitable. However, the proposed oscillator does not use the current source, so the minimum noise factor is obtained. As a result, the phase noise up to 1MHz offset frequency has improved more than 10dB. There is a little hump in the middle offset frequency. That is contributed by the off-chip voltage regulator for power supply and bias voltage. When the power supply was directly connected for V_{DD} and bias, there was larger hump. But, it is decreased when they are passed through the voltage regulator. It means that this hump is from off-chip regulator, not from the oscillator itself. The phase noise at higher than 1MHz offset frequency is larger than the conventional Colpitts oscillator. The far out offset frequency is mainly contributed by either output amplitude or noise from output buffer. When I taped out the conventional Colpitts oscillator, I had enough area to use to put another same oscillator for test purpose and only one open drain buffer was used. The output amplitude of it was around -9dBm. But, for the recent tape out, the transformer coupled oscillator was used for BLE receiver system. As there was insufficient area to put one more oscillator, the output was pulled out from the system through buffer chain. Those harsh test environment contributes to higher phase noise at a far out offset frequency.

To clarify the phase noise improvement at close-in offset frequency, V_{DD} of the oscillator is changed. Figure 61 shows how the phase noise changes when V_{DD} varies from 1V to 0.65V. The amplitude of the output signal changes proportionally to the V_{DD} value in general. That's why phase noise at 10MHz offset improves as V_{DD} increases. However, close-in phase noise is consistent no matter what V_{DD} value is. Figure 61 represents the same in detail.

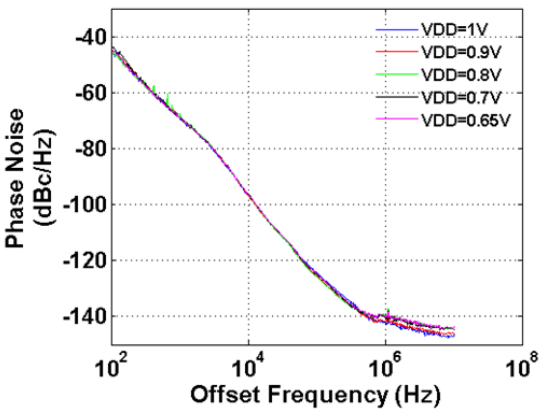

Figure 61: Phase Noise Plot with V_{DD} Change

2.12.1.1 Oven Controlled Temperature Compensation System

Figure 62 represents the approach of this work. It uses the sensor integrated in the same resonator chip in order to monitor its temperature. Basically, a sensor is the resistor implemented by MEMS technology. Its resistance varies according to the changes in temperature. Temperature-to-digital converter (TDC) detects such resistance variations in real time and converts them to digital values consisting of 21 bit bus. This 21bits digital value represents the temperature of the resonator chip. The following digitally implemented integrator compares this with the target temperature value and accumulates the difference. If the temperature of the resonator chip is equal to the target, the difference of these two will decrease, and it eventually reaches '0'. Then, the accumulation will be stopped.

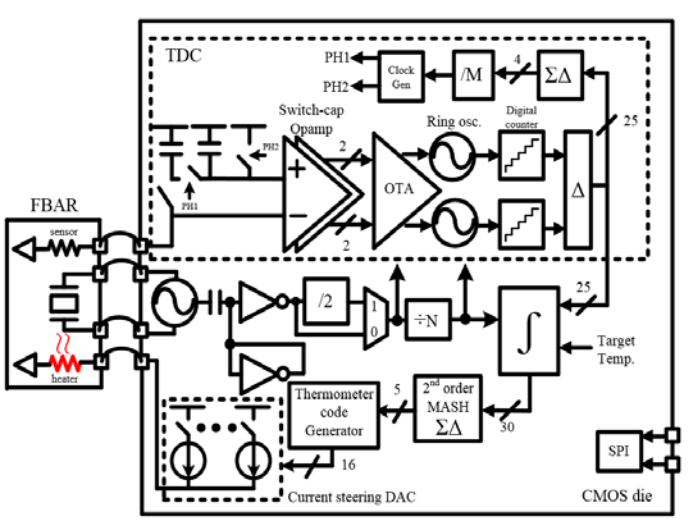

Figure 62: Block Diagram of the Oven Controlled Temperature Compensation System

The output of the accumulator consisting of 40 bits cannot be directly connected to the current steering DAC. That's because the number of current source needed to be implemented would be 2^{40} if thermometer code is utilized to get low integral nonlinearity (INL) and differential nonlinearity (DNL) errors. It requires a huge

area as well as large power consumption. Even if the binary control is used and 40 current sources are used, there will be other issues such as a mismatch between current sources and increased INL and DNL errors. That's why the 2nd order mesh type sigma delta modulator is used to change 40 bits to 4 bits, maintaining the average value of 4 bits in real time equal to an input of 40 bits. It allows the current steering DAC to have only 2^{16} current source with thermometer code control.

The current steering DAC can generate the output current up to 12mA to cover high temperature (80°C) with ±0.15 LSB DNL and INL errors. TDC shows superior resolution (150uK) compared to other temperature sensors. As it is a negative feedback structure, it does not need calibration for the resonator chip. This lowers the test time and its time-to-market. From the following sections, each blocks will be described in more detail considering each test result.

2.12.1.2 Temperature to Digital Converter

One of the key blocks for temperature compensation system is the TDC. Figure 63 shows its entire block diagram. The front-end circuit consists of a resistive bridge that is balanced by digitally tuning a switch capacitor resistor. The resistance of the switch capacitor changes according to the frequency of the clock, clk_ph1 and clk_ph2 in the figure. The comparison of R1, sensor resistance, and switch capacitor is achieved by using a CMOS switch (sw1) to periodically short them together at 32 kHz frequency. This 32 kHz frequency clock is derived from FBAR based oscillator output.

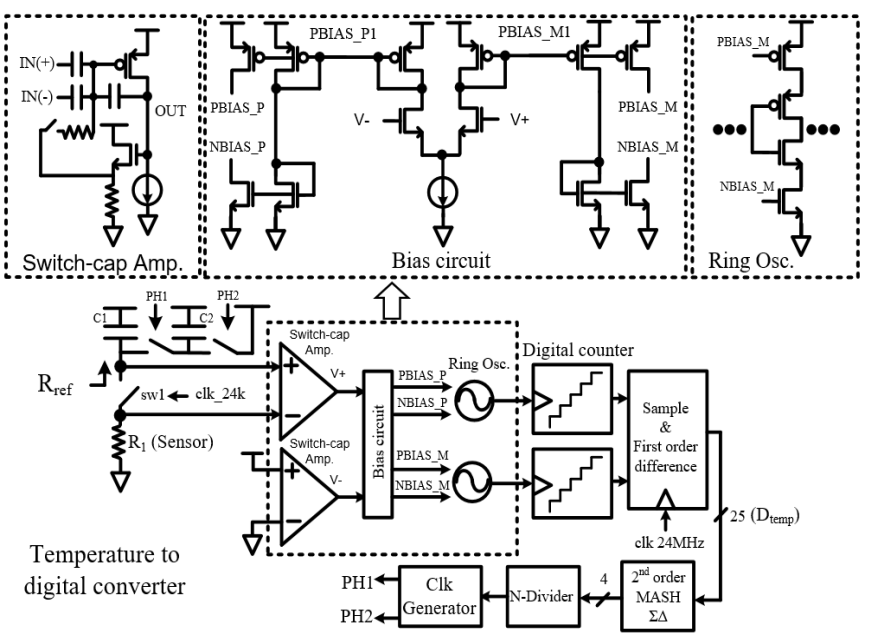

Figure 63: Block Diagram of Temperature to Digital Converter

In the steady state, both the sensor and switch capacitor resistance become equal, and the voltage of middle node becomes $V_{DD}/2$ when the switch (sw1) is closed. If there is a temperature change, the resistance of sensor will vary and the voltage of middle node will deviate from $V_{DD}/2$. Then, the amount of deviation will

be amplified by the switch capacitor amplifier. Operational transconductance amplifier (OTA) changes the output voltage of switch capacitor amplifier to current. This current feeds to the current starving ring oscillator. Two ring oscillators are used. After sampling, the count values are compared with the previous values such that a fist-order difference operation is achieved. So, effectively, quantized frequency difference between the oscillators is obtained. This quantized digital value consisting of 25 bits bus represents the temperature information on the resonator chip. The equation below represents the relationship between resistance of switch capacitor (R_{ref}), digital value (D_{temp}) and clock frequency (PH1, PH2).

$$R_{ref} = \frac{T_{PH1}}{C_2} D_{temp} \tag{12}$$

According to its value, clk generator block on the figure controls the frequency of both PH1 and PH2. To reduce the complexity of design, the 2nd order multi-stage noise shaping (MASH) type sigma delta modulator is used. This decreases the number of bits from 25 bits to 4 bits. The average value of 4 bits output is the same with its 25 bits input value. The detailed structure of sigma modulator will be shown later.

AlN CMR device is also used as a sensor for TDC test to check if TDC functionality is same. Figure 64 shows die photo. After the device is fabricated by Carnegie Mellon University MEMS fab, the resonator is exposed to air. So, we cannot get each device because chip can be damaged during dicing process. That's why AlN CMR chip has huge size and only one of them is connected through wire.

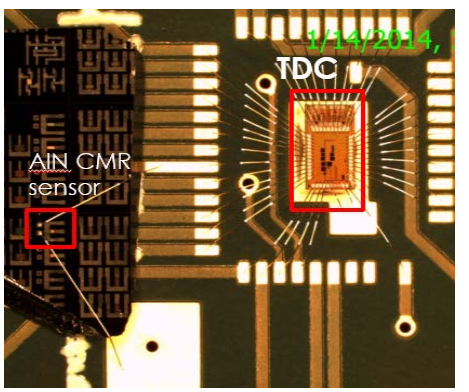

Figure 64: Die Photo of TDC Connected to AlN CMR

Figures 65 and 66 represents block diagram showing two types test set up. One is that I put only AlN CMR sensor inside the chamber and change the temperature from -40°C to 100°C. The purpose of this set up is for checking how wide the resistance of AlN CMR sensor varies. As shown in Figure 65, TDC can maintain a good linearity over a wide temperature range.

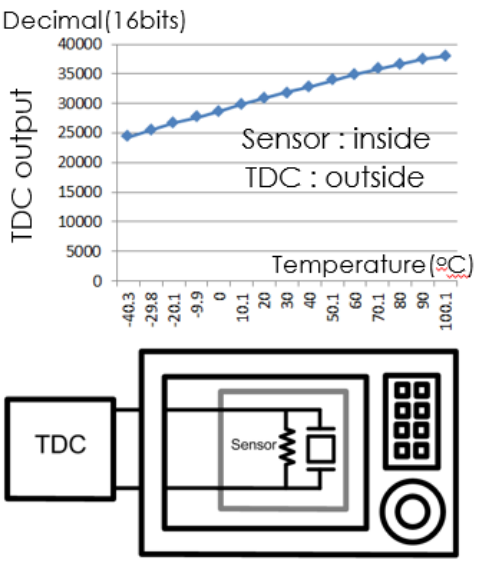

Figure 65: Test Set Up with Sensor inside Chamber

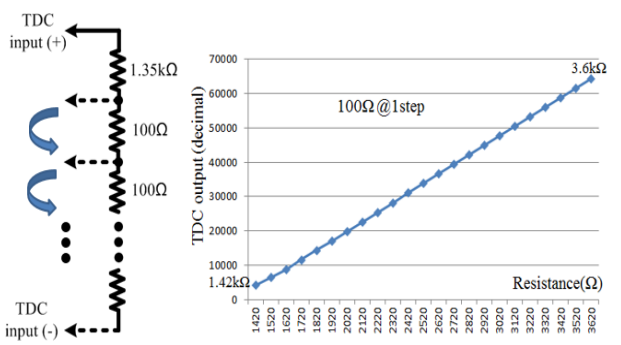

Figure 66: Test Set Up with all Test Chips Inside

The other characteristic of TDC I need to test is its detection range. There must be lowest and highest resistance values which TDC can detect. For this check, I had built a bunch of off-chip resistors connected in series as shown in Figure 66. The default resistance connected to TDC is 1.35kohm. Resistance can be increased by moving one of the taps connected to TDC next to the resistor. In this test set up, I can increase the resistance by 100ohm. To sum up, the TDC can detect resistance from 1.5kohm to 3.6kohm. If either the FBAR or AlN CMR sensor changes within this range over temperature change, TDC will have no issue for its functionality.

2.12.1.3 Current Steering DAC

Figure 67 shows the current steering DAC which is robust to high V_{DD} and has higher accuracy. It shows that the output stage is directly connected to the heater through wire-bonding. The mechanism of operation is similar to 1st prototype. 17 number of current sources are used. As the digital input value varies by the thermometer control, the same amount of current sources are used. When the current sources are turning on

sequentially, the voltage of the node which sums up all current changes as the output impedance looking at turned-on current sources decrease. It degrades the INL and DNL errors. Therefore, opamp (OP1) and M3 thick devices are used to maintain the output voltage of the current source to a certain value. This results in high output impedance leading to low DNL and INL errors.

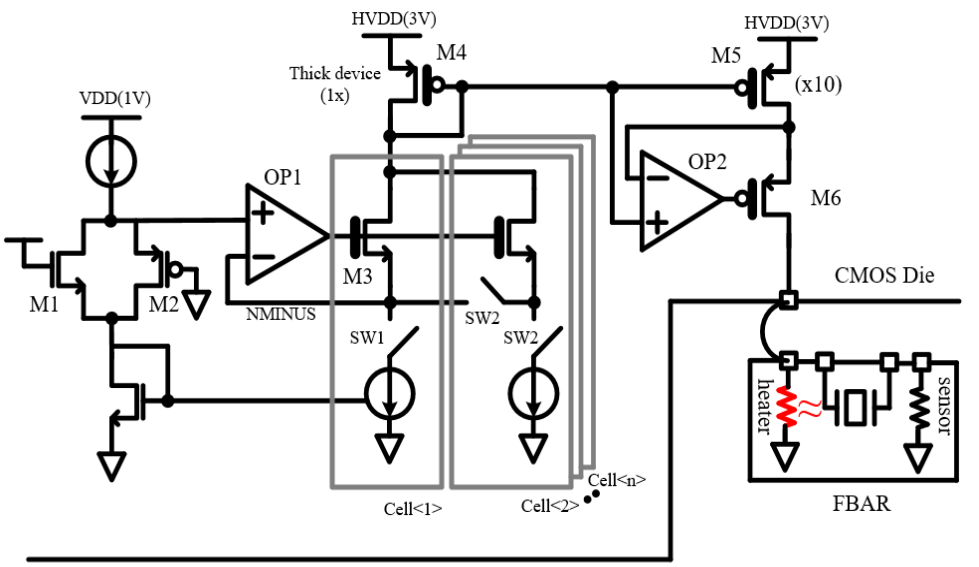

Figure 67: Block Diagram of the Current Steering DAC

The shift register can be programmed to feed the input data manually; the output current flowing through the heater can be monitored. The DAC is tuned to have 3.5mA of maximum output current first. Figure 68 shows how the output current changes according to the input data. For the comparison purpose, simulation result is also plotted in the same chart. As you can see, the test result exactly matches with the simulation result. At the maximum input, the amount of current is slightly deviated from the ideal value (50uA), but its accuracy is high enough. We can see the characteristic of DAC more clearly in terms of its error by using INL and DNL as shown in Figure 69. The maximum error is 0.25 LSB which is lower than 1st prototype DAC (0.4 LSB).

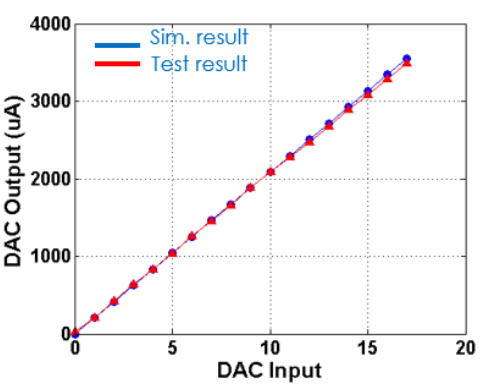

Figure 68: Test Result of the Current Steering DAC

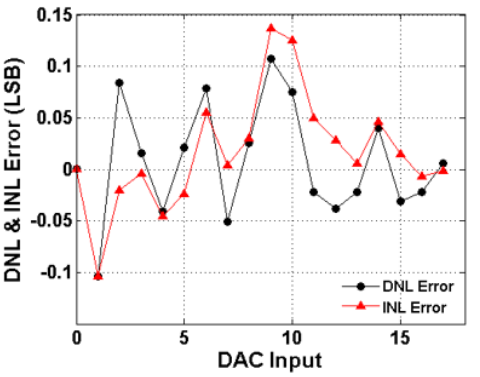

Figure 69: INL and DNL of the Current Steering DAC

AlN CMR device has two spurious modes as shown in Figure 69 and cannot have fixed characteristics for constructing MBVD model. Therefore, it was difficult to optimize the transformer coupled oscillator. Fortunately, when I taped out the system, the capacitor array is integrated to make the oscillator work either with FBAR or AlN CMR. Thus, FBAR is used for temperature compensation system test. Figure 70 shows the die photo of the system chip wirebonded with FBAR. The sensor and heater are connected to the TDC front-end and current steering DAC output respectively through PCB boards. For more information, heater resistance is around 120 ohm and sensor has 2kohm resistance which is within the TDC detection range.

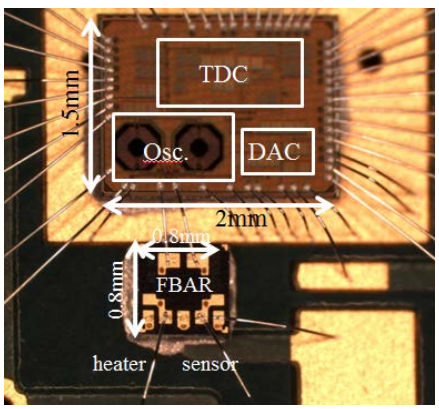

Figure 70: Die Photo of the System

Figure 71 shows the frequency drift of the oscillator over the temperature change with system on and off. The blue graph represents how much the frequency varies when the system is off. The overall frequency change is around 300ppm which is larger than I expected. When the system is turned on and the shift registers are programmed to have the target temperature of 20^{o}C, red curve shows that the frequency is stable until temperature reaches to 20^{o}C. When the target temperature is set to 80^{o}C, the oscillator output clock is stable until it reaches the target temperature. Figure 72 shows the detail test result of both low target temperature (20^{o}C) and high target temperature (80^{o}C). As shown in this plot, the maximum frequency drift is ±1.55ppm.

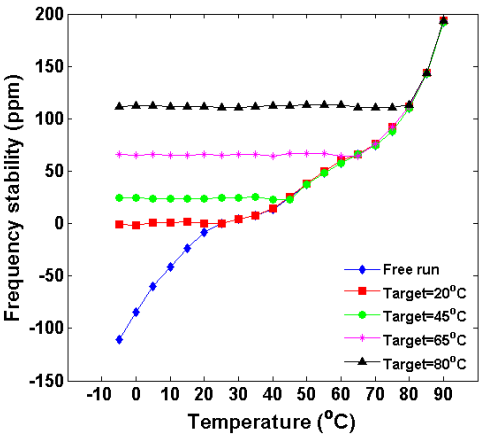

Figure 71: Frequency Drift of the Oscillator over the Temperature Change with System On and Off

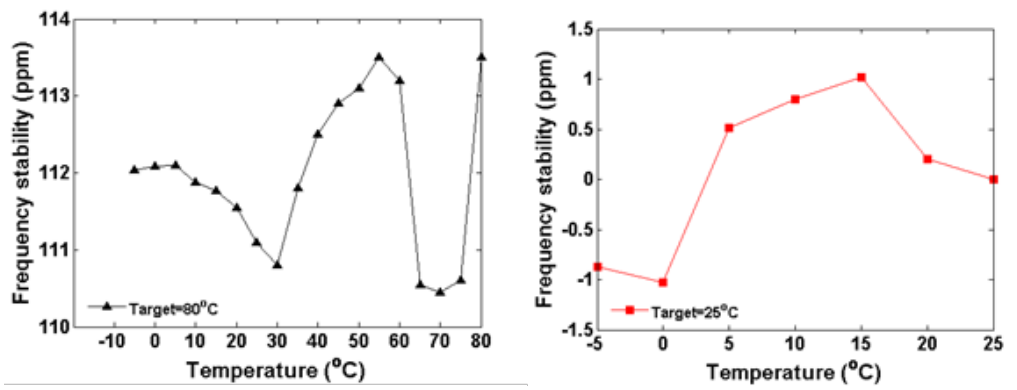

Figure 72: Frequency Stability when the Target Temperature is set to 80°C (left) and 20°C (right)

It is interesting to see how the output current from current steering DAC changes when the temperature varies with various target temperatures. Figure 73 shows such results. When the target is programmed to have 80°C and the current temperature of the chip is -5°C, the maximum current, in this case 12mA, is required to generate heat for 80°C. As the temperature inside the chamber increases, you can see that the output current from DAC decreases.

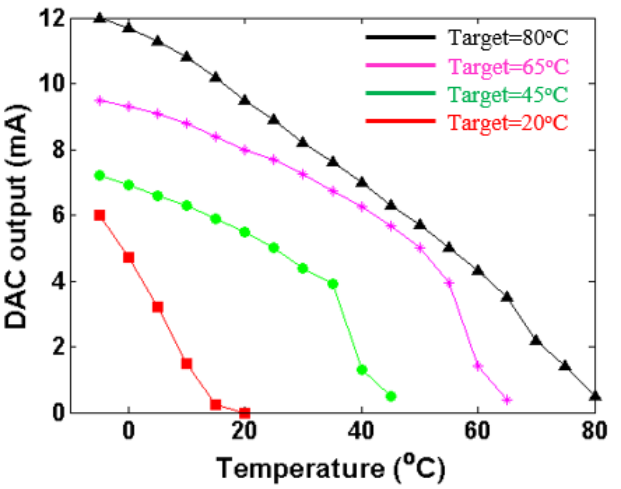

Figure 73: Output Current Variation of the DAC over Temperature Change with Various Target Setting

This oven controlled temperature compensation system is the first fully integrated work fabricated by 65nm CMOS technology with a size of 1.5mm x 2mm. The best test result (±1.55ppm) is obtained when 980mV V_{DD} and a half frequency of the clock from oscillator are used for the system. The power consumption of the oscillator is only 250uW and 2.9mW is required for the other blocks. Compared to other state-of-the art temperature sensors, it achieves highest resolution (150uK). The other benefit is that it does not need calibrations for FBAR as it is a feedback system.

3.0 CONCLUSION AND FUTURE DIRECTION

The reference clock is an essential component in most electronic systems. That's why there are always specific requirements such as temperature characteristics and short-term frequency fluctuation (phase noise). These days each person is using at least more than one portable device and people connect with each other through wireless communication. Since the amount of data and their speed keep increasing, the environment for such wireless systems is getting increasingly stringent and harsher. More specifically, the noise skirt from reference clock affects the signal integrity of both transceiver and receiver leading to a limiting channel space.

Besides the phase noise requirement in wireless applications such as Wi-Fi, Bluetooth, and GPS, frequency stability under temperature change is also a very important specification that needs to be satisfied. Although the introduced oscillator using MEMS based resonator helps to lower phase noise and achieve high FOM compared to other state-of-the art oscillators, the resonator is the main contributor for frequency variation according to the temperature change. This thesis demonstrated the first fully integrated oven control system to mitigate the temperature effect on the reference clock. It showed low frequency drift (1.5ppm) with the highest resolution sensor (150uK), which meets the most stringent requirement for GPS application. As this system does not require any calibration on the MEMS resonator because of its feedback structure, we can benefit from its characteristics of short test time and time-to-market. It can also lead to lower cost from the product perspective.

During the work, we found that there are multiple spurious modes in the resonator leading to have a difficult time to optimize the oscillator. The oscillator showed different phase noise performance according to where it works among those modes. So, in the near future, we need to investigate more to design and make the oscillator controllable in order to investigate the phase noise of it.

3.1 Acceleration Sensitivity

The measurement of the acceleration sensitivity (Figure 74) clearly highlights its dependence on factors other than the intrinsic resonator out-of-plane displacement. The oscillator Γ is well below the Phase II metric (< 30 ppb/G for all vibration frequencies), but shows a linear dependence on the vibration frequency, which is likely indicative of poorly mounted components or wirebond vibrations. If we consider the vibration frequency of 2 kHz, we can see how our existing oscillator meets Phase III specifications.

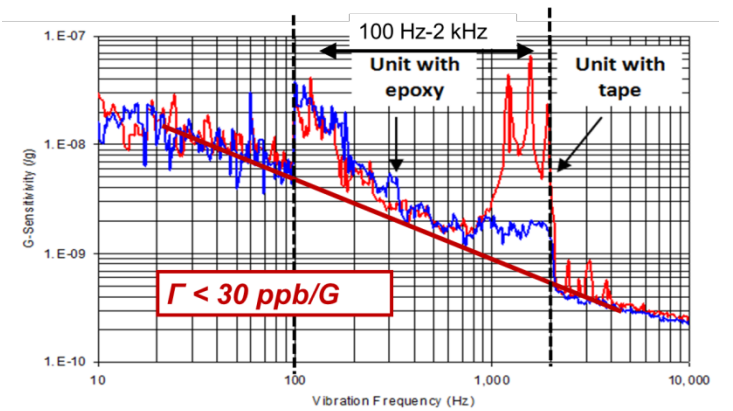

Figure 74: Acceleration Sensitivity Testing Performed at Vectron on a Temperature Compensated Unit

The acceleration sensitivity is < 30 ppb/G for all vibration frequencies. It is clear that component mounting plays a key role as just epoxying some of the components reduces spurious peaks in the sensitivity plot.

4.0 PUBLICATIONS

4.1 Journal Publications

1. S. Ghosh and G. Piazza, "*Piezoelectric actuation of aluminum nitride contour mode optomechanical resonators*," Optics Express, 23, p. 15477, 2015.
2. C. Cassella and G. Piazza, "*AlN Two-Dimensional-Mode Resonators for Ultra-High Frequency Applications*," IEEE Electron Device Letters, 36(11), p. 1192-1194, 2015
3. J. Segovia, M. Cremonesi, A. Frangi, and G. Piazza, "*Anchor Losses in AlN Contour-Mode Resonators*", Journal of Microelectromechanical Systems, 24(2), p. 265-275, 2015.
4. C. Cassella and G. Piazza, "*Low Phase Noise Autonomous Parametric Oscillator based on a 226.7 MHz AlN Contour-Mode Resonator*," IEEE Transactions on Ultrasonics, Ferroelectrics and Frequency Control, 62(4), p. 617-624, 2015.
5. N. Miller, and G. Piazza, "*Measurements of Frequency Fluctuations in Aluminum Nitride Contour-Mode Resonators*", IEEE Transactions on Ultrasonics, Ferroelectrics and Frequency Control, 61(6), p. 913-919, 2014.
6. N. Miller and G. Piazza, "*Nonlinear dynamics in aluminum nitride contour-mode resonators*", Applied Physics Letters, 104(1), p. 014102, 2014.
7. J. Segovia-Fernandez and G. Piazza, "*Thermal Nonlinearities in Contour Mode AlN Resonators*", Journal of Microelectromechanical Systems, 22(4), p. 976-985, 2013.
8. A. Tazzoli, M. Rinaldi, and G. Piazza, "*Experimental Investigation of Thermally Induced Nonlinearities in Aluminum Nitride Contour-Mode MEMS Resonators*", IEEE Electron Device Letters, 33(5), p. 724-726, 2012.
9. Z. Yie, M. A. Zielke, C. B. Burgner, and K. L. Turner, "*Comparison of Parametric and Linear Mass Detection In the Presence of Detection Noise"*, Journal of Micromechanics and Microengineering, 21, p. 025027, 2011.

4.2 Conference Publications

1. B. Gibson, K. Qalandar, G. Piazza, and K. Turner, "*A Novel Method for Measuring Ring-Down in a High Noise and High Frequency System Using Laser Doppler Vibrometery*," Solid-State Sensors, Actuators and Microsystems Workshop (Hilton Head 2016), accepted, 2016
2. H.J. Kim, J. Segovia-Fernandez, and G. Piazza, "*Damping Directly Impacts Flicker Frequency Noise of Piezoelectric Aluminum Nitride Resonators*," IEEE 29th International Conference on Micro Electro Mechanical Systems (MEMS 2016), accepted for publication, 2016
3. S. Ghosh and G. Piazza, "*Elasto-Optic Modulator Integrated in High Frequency Piezoelectric MEMS Resonators*," IEEE 29th International Conference on Micro Electro Mechanical Systems (MEMS 2016), accepted for publication, 2016
4. J. Segovia-Fernandez and G. Piazza, "*An Alternative Technique to Perfectly Matched Layers to Model Anchor Losses in MEMS Resonators with Undercut Suspensions*," Transducers & Eurosensors XXVII: The 18th International Conference on Solid-State Sensors, Actuators and Microsystems (TRANSDUCERS & EUROSENSORS XXVIII), p. 985-988, 2015.
5. C. Xu, J. Segovia-Fernandez, and G. Piazza, "*Sub-milliwatt Integrated Oven for Temperature Stable Laterally Vibrating Piezoelectric MEMS Resonators*," Transducers & Eurosensors XXVII: The 18th International Conference on Solid-State Sensors, Actuators and Microsystems (TRANSDUCERS & EUROSENSORS XXVIII), p. 977-980, 2015.

6. S. Ghosh, J. Segovia-Fernandez, and G. Piazza, "*Piezoelectrically-Actuated Opto-Acoustic Oscillator*," 2015 Joint Conference of the IEEE International Frequency Control Symposium & European Frequency & Time Forum (IFCS-EFTF 2015), p. 72-75, 2015,.

7. B. Gibson, K. Qalandar, K. Turner, C. Cassella, and G. Piazza, "*Analysis of the impact of release area on the quality factor of contour-mode resonators by laser Doppler vibrometry*," Joint European Frequency and Time Forum & International Frequency Control Symposium (EFTF/IFC), p. 709-712, 2015.

8. J. Segovia-Fernandez, and G. Piazza, "*Damping in 1 GHz Laterally-Vibrating Composite Piezoelectric Resonators*," IEEE 28th International Conference on Micro Electro Mechanical Systems (MEMS 2015), p. 1000-1003, 2015.

9. C. Cassella, M. Cremonesi, A. Frangi, and G. Piazza, "*Q optimization via λ/4 acoustic transformers in the body of AlN contour-mode resonators*", Solid-State Sensors, Actuators and Microsystems Workshop (Hilton Head 2014), p. 427-430, 2014.

10. N. Saldhana, U. Zaghloul, and G. Piazza, "*Residual Noise Reduction in AlN Resonators by Prolonged RF Excitation*", IEEE International Frequency Control Symposium (FCS), p. 552-555, 2014,.

11. C. Cassella and G. Piazza, "*Parametric Filtering Surpasses Resonator Noise in AlN Contour-Mode Oscillators*", IEEE 27th International Conference on Micro Electro Mechanical Systems (MEMS 2014), p. 1269-1272, 2014.

12. J. Koo, A. Tazzoli, J. Segovai-Fernandez, G. Piazza, and B. Otis, "*A− 173 dBc/Hz@ 1 MHz offset Colpitts oscillator using AlN contour-mode MEMS resonator*", IEEE Custom Integrated Circuits Conference (CICC), p. 1-4, 2013.

13. J. Segovia-Fernandez, C. Cassella, and G. Piazza, "*Close-in phase noise reduction in an oscillator based on 222 MHz non-linear contour mode AlN resonators*", Joint European Frequency and Time Forum & International Frequency Control Symposium (EFTF/IFC), p. 13-16, 2013. *Best student paper award in Group 1*.

14. G. Piazza, A. Tazzoli, N. Miller, J. Segovia, C. Cassella, J. Koo, B. Otis, K. McNaul, B. Gibson, and K. Turner, "*Dynamics of microscale thin film AlN piezoelectric resonators enables low phase noise UHF frequency sources*", Joint European Frequency and Time Forum & International Frequency Control Symposium (EFTF/IFC), p. 555-558, 2013.

15. N. Miller and G. Piazza, "*Nonlinear dynamics in aluminum nitride contour-mode resonators*", Joint European Frequency and Time Forum & International Frequency Control Symposium (EFTF/IFC), p. 9-12, 2013

16. N. Miller and G. Piazza, "*Vector network analyzer measurements of frequency fluctuations in aluminum nitride contour-mode resonators*", Joint European Frequency and Time Forum & International Frequency Control Symposium (EFTF/IFC), p. 666-669, 2013.

17. C. Cassella, J. Segovia-Fernandez, G. Piazza, M. Cremonesi, and A. Frangi, "*Reduction of anchor losses by etched slots in aluminum nitride contour mode resonators*", Joint European Frequency and Time Forum & International Frequency Control Symposium (EFTF/IFC), p. 926-929, 2013.

18. J. Segovia-Fernandez, M. Cremonesi, C. Cassella, A. Frangi, and G. Piazza, "*Experimental study on the impact of anchor losses on the quality factor of contour mode AlN resonators*", Transducers & Eurosensors XXVII: The 17th International Conference on Solid-State Sensors, Actuators and Microsystems (TRANSDUCERS & EUROSENSORS XXVII), p. 2473-2476, 2013.

19. C. Cassella, J. Segovia-Fernandez, and G. Piazza, "*Segmented electrode excitation of aluminum nitride contour mode resonators to optimize the device figure of merit*", Transducers & Eurosensors XXVII: The 17th International Conference on Solid-State Sensors, Actuators and Microsystems (TRANSDUCERS & EUROSENSORS XXVII), p. 506-509, 2013,.

20. A. Tazzoli, G. Piazza, "*Low Power Consumption, Temperature, and Acceleration Insensitive Clocks Based on Ovenized UHF AlN MEMS Resonator*", INVITED paper at 22nd Workshop on Advances in Analog Circuit Design, Grenoble, France, 2013

21. A. Tazzoli, N.-K. Kuo, M. Rinaldi, H. Pak, D. Fry, D. Bail, D. Stevens, Gianluca Piazza, "*A 586 MHz Microcontroller Compensated MEMS Oscillator Based on Ovenized Aluminum Nitride Contour-Mode Resonators*", Proceedings of the IEEE International Ultrasonics Symposium (IUS), 2012

22. J. S.-Fernandez, N.-K. Kuo, G. Piazza, "*Impact of Metal Electrodes on the Figure of Merit (kt2·Q) and Spurious Modes of Contour Mode AlN Resonators*", Proceedings of the IEEE International Ultrasonics Symposium (IUS) p. 299-302, 2012.

23. M. Rinaldi, A. Tazzoli, C. Zuniga, G. Piazza, "*970 MHz Ovenized Oscillator based on an AlN MEMS Resonator with Monolithically Integrated Suspended Nano Hot Plate*", *Proceedings of the 2012 Solid-State Sensors, Actuators and Microsystems Workshop (Hilton Head 2012)*, Hilton Head Island, p. 347-350, 2012.

24. A. Tazzoli, M. Rinaldi, G. Piazza, "*Ultra High Frequency Temperature Compensated Oscillators Based on Ovenized AlN Contour-Mode MEMS Resonators*", *IEEE International Frequency Control Symposium (IFCS)*, p. 1-5, *2012*.

25. M. Rinaldi, C. Zuniga, A. Tazzoli, G. Piazza, "*High Frequency AlN MEMS Resonators with Integrated Nano Hot Plate for Temperature Controlled Operation*", *IEEE International Frequency Control Symposium (IFCS)*, 2012.

26. A. Tazzoli, G. Piazza, M. Rinaldi, J. Segovia, C. Cassella, B. Otis, J. Shi, K. Turner, C. Burgner, K. McNaul, D. Bail, V. Felmetsger, "*Piezoelectric Non-Linear Nanomechanical Temperature and Acceleration Insensitive Clocks*", Invited paper at SPIE 2012, 83730A, 2012.

27. M. Rinaldi, A. Tazzoli, J. Segovia, V. Felmetsger, G. Piazza, "*High Power and Low Temperature Coefficient of Frequency Oscillator Based on a Fully Anchored and Oxide Compensated AlN Contour-Mode Resonator*", IEEE MEMS 2012, p. 696– 699, January 2012.

28. A. Tazzoli, M. Rinaldi, C. Zuo, N. Sinha, J. V. der Spiegel, G. Piazza, *"Aluminum Nitride Reconfigurable RF-MEMS Front-Ends"*, INVITED paper at ASICON 2011, p. 1046 – 1049, 2011.

29. A. Tazzoli, M. Rinaldi, G. Piazza, "*Ovenized High Frequency Oscillators Based on Aluminum Nitride Contour Mode MEMS Resonators*", IEEE IEDM 2011, p. 20.2.1-20.2.4, 2011.

30. J. S.-Fernandez, A. Tazzoli, M. Rinaldi, G. Piazza, *"Nonlinear lumped electrical model for Contour Mode AlN Resonators"*, Proc. of IEEE International Ultrasonics Symposium, p. 1846 – 1849, 2011.

31. G. Piazza, A. Tazzoli, N. Miller, J. Segovia, C. Cassella, J. Koo, B. Otis, K. McNaul, B. Gibson, and K. Turner, "*Dynamics of microscale thin film AlN piezoelectric resonators enables low phase noise UHF frequency sources*," Joint European Frequency and Time Forum & International Frequency Control Symposium (EFTF/IFC), p. 555-558, 2013.

32. C. B. Burgner, L. A. Shaw, and K. L. Turner, "*A New Method For Resonant Sensing Based on Noise In Nonlinear Mems*," IEEE 25th International Conference on Micro Electro Mechanical Systems (MEMS 2012), p. 511-514, 2012.

33. C. B. Burgner, W. S. Snyders, and K. L. Turner, "*Control of MEMS on the Edge of Instability*," in Transducers , 16th International Solid-state Sensors, Actuators and Microsystems Conference (TRASNDUCERS), p. 1990-1993, 2011.

34. K.L.Turner, C.B. Burgner, Z. Yie, E. Holtoff "*Using nonlinearity to enhance micro/nanosensor performance*," INVITED paper at IEEE Sensors, p. 1-4, 2012.

LIST OF SYMBOLS, ABBREVIATIONS, AND ACRONYMS

ACRONYM	DESCRIPTION
AFRL	Air Force Research Laboratory
AlN	aluminum nitride
AM-PM	amplitude modulation to phase modulation
CMOS	complementary metal-oxide semiconductor
CMR	contour mode resonator
CW	continuous wave
DAC	digital-to-analog converter
DARPA	Defense Advanced Research Agency
DC	direct current
DNL	differential nonlinearity
FBAR	film bulk acoustic resonator
FEA	finite element analysis
FEM	finite element method
FET	field-effect transistor
FOM	figure of merit
INL	integral nonlinearity
LDV	Laser Doppler Vibrometer
MASH	multi-stage noise shaping
MBVD	Modified Butterworth Van Dyke
MEMS	microelectromechanical systems
OCXO	oven-controlled crystal oscillator
OTA	operational transconductance amplifier
PCB	printed circuit board
PML	perfectly matched layer
PN	phase noise
PSD	power spectral density
RC	resistor-capacitor
RF	radio frequency
SAW	surface acoustic wave
SSB	single sideband
TCF	temperature coefficient of frequency
TCXO	temperature compensated crystal oscillator
TDC	temperature-to-digital converter
TED	thermoelastic damping
TSMC	Taiwan Semiconductor Manufacturing Company
UHF	ultra-high frequency
VNA	vector network analyzer